SURFACE ADSORPTION AND RESONANCE IONIZATION SPECTROSCOPY FOR BARIUM IDENTIFICATION IN NEUTRINOLESS DOUBLE BETA DECAY EXPERIMENTS

A DISSERTATION
SUBMITTED TO THE DEPARTMENT OF PHYSICS
AND THE COMMITTEE ON GRADUATE STUDIES
OF STANFORD UNIVERSITY
IN PARTIAL FULFILLMENT OF THE REQUIREMENTS
FOR THE DEGREE OF
DOCTOR OF PHILOSOPHY

Karl Twelker
August 2014

I certify that I have read this dissertation and that, in my opinion, it is fully adequate in scope and quality as a dissertation for the degree of Doctor of Philosophy.

Giorgio Gratta, Primary Adviser

I certify that I have read this dissertation and that, in my opinion, it is fully adequate in scope and quality as a dissertation for the degree of Doctor of Philosophy.

Patricia Burchat

I certify that I have read this dissertation and that, in my opinion, it is fully adequate in scope and quality as a dissertation for the degree of Doctor of Philosophy.

Peter Graham

Approved for the Stanford University Committee on Graduate Studies.

Patricia J. Gumport, Vice Provost for Graduate Education

This signature page was generated electronically upon submission of this dissertation in electronic format. An original signed hard copy of the signature page is on file in University Archives.

Abstract

Neutrinos are the only elementary particle that could have particle-antiparticle duality, called Majorana nature. If neutrinos do indeed have this property, it could be measured through neutrinoless double-beta decay, a hypothetical nuclear decay. The half-life of this decay is very long, thus the reduction of backgrounds is very important. In searches for neutrinoless double-beta decay in ^{136}Xe, backgrounds in the signal region of interest can be eliminated by recovering the expected daughter nucleus of this decay, ^{136}Ba. This work describes the development of a technique to recover these barium ions from liquid xenon using surface adsorption and identify them using Resonance Ionization Spectroscopy (RIS). Barium ions adsorb onto a surface in the liquid xenon, which we remove to a separate vacuum chamber for identification. Laser induced thermal desorption removes atoms from the surface into vacuum, then the barium is re-ionized using RIS and drifted down a time of flight mass spectrometer. RIS has been shown to be both efficient and selective, both favorable aspects for a barium tagging system. The prototype system described here offers both optical spectroscopic and mass spectroscopic confirmation of the barium daughter. Barium tagging is being developed for use in nEXO, a future neutrinoless double-beta decay experiment, and will allow the detector to probe into the normal hierarchy of neutrino masses.

Acknowledgement

Many have helped me with all aspects of my graduate career, there have been too many to make a complete listing here. First and foremost, Giorgio Gratta has supported me on this project through many puzzling datasets. Those puzzling datasets and the countless modifications of the device have developed my confidence and ability as an experimentalist. Bill Fairbank shared with us his wealth of knowledge related to desorption and RIS. Without his advice, we would not have made this progress. Thanks also to María Montero Díez for laying the solid foundation upon which this work is based, and to Scott Kravitz for helping with the construction and operation of the device as well as with the interpretation of the data. He will continue to bring this project to new heights.

All members of the Gratta group during my time helped work through designs and problems with the device. I greatly appreciate all of their help, advice, and friendship. Everyone in the group has contributed to my success and development in graduate school. In particular, Thomas Brunner and Alexis Schubert helped with the writing of this thesis. Working within the EXO collaboration has been fun and challenging, thanks to all of my collaborators who broadened my view of physics and the world, as well as for their advice and encouragement on this project. Outside of this core group, I have consulted with many others on surface science, including Hari Manoharan, Jared Schwede and Astrid Tomada.

The construction of the device would not have been possible without the help of the physics machine shop crew: Karlheinz Merkle, Mehmet Solyali, John Kirk, Matt Chuck and Scott Barton all built parts of the experiment. Bob Conley helped with the welding and brazing on almost every single part of the apparatus.

I would also like to thank my grad school friends for their involvement, encouragement and commiseration. There's nothing quite like a violent game of backyard water polo to release the stresses of lab. I've also shared many rides, car trips, and race weekends with the Stanford Cycling team. Nathaniel Craig has been a particularly strong influence on both my physics and my cycling, I've appreciated his company throughout graduate school.

Thanks to my parents, Janeann and Eric, and my brother Evan for supporting me throughout this. I could not have gotten here without you. Finally, thanks to Susannah Dickerson, who has been my best friend and support crew through grad school and into whatever comes next.

Contents

List of Tables

List of Figures

Chapter 1

Neutrino Mass and $\beta\beta$ Decay

Neutrinos are common particles in the universe; however, measurements of their properties remain an open challenge for experimentalists due to their very small mass and weak interaction with matter. Three flavors of neutrinos have been detected: ν_e, ν_μ, ν_τ, corresponding to the three Standard Model generations of charged leptons [1].

While the Standard Model originally assumed neutrinos were massless, neutrino oscillation experiments have found that neutrinos have a finite but very small mass. Evidence of neutrino mass has also opened the possibility that neutrinos are their own antiparticle, a so-called *Majorana* particle [2]. The neutrino is the only known elementary particle that is potentially a Majorana particle. This leads to two large open questions in neutrino physics: What is the absolute mass of neutrinos? And is the neutrino a Majorana fermion?

The first question, concerning the mass of the neutrino, is complicated by the fact that the mass eigenstates are distinct from the flavor eigenstates. The neutrino mass eigenstates gain definite masses through interactions with the Higgs field, however these mass eigenstates are not eigenstates of flavor which determine neutrino interactions with matter. Neutrinos created in a flavor eigenstate are in fact a linear combination of the mass eigenstates. The probability of detecting a given flavor eigenstate is determined from the energy and distance from the neutrino source [3]. The Pontecorvo-Maki-Nakagawa-Sakata (PMNS) matrix U describes the projection

from flavor eigenstates ($|\nu_\alpha\rangle$) onto mass eigenstates ($|\nu_i\rangle$) [1],

$$|\nu_\alpha\rangle = \sum_i U^*_{\alpha i}|\nu_i\rangle. \tag{1.1}$$

This matrix can be parameterized in terms of three neutrino mixing angles (θ_{12}, θ_{13}, θ_{23}) and three phase factors (δ, α_{21}, α_{31}). The phase factor δ is related to CP violation, while α_{21} and α_{31} could be observable if the neutrino is a Majorana particle, described below. Oscillation experiments are able to measure the neutrino mixing angles as well as the differences in masses between mass eigenstates, but they cannot measure the absolute scale of neutrino masses.

Analyses of solar neutrino oscillations have determined one mass difference to be positive due to the matter effect in the sun: $m_2 > m_1$ [1]. However, it is not yet known if m_3 is heavier or lighter than this pair. Since the sign of this mass difference is unknown, neutrino masses can have one of two orderings, which are called the normal and the inverted mass hierarchies. This is referred to as the neutrino hierarchy problem. In the normal hierarchy, the mass difference is such that m_3 is larger than the pair of masses m_1 and m_2, while in the inverted hierarchy m_3 is less than the m_1, m_2 pair. These mass differences (defined as $\Delta m^2_{ij} = m^2_i - m^2_j$) are measured to be $\Delta m^2_{21} = 7.62^{+0.19}_{-0.19} \times 10^{-5}$ eV^2, and $\Delta m^2_{31} = 2.55^{+0.06}_{-0.09} \times 10^{-3}$ eV^2 (normal hierarchy) or $\Delta m^2_{31} = -2.43^{+0.07}_{-0.06} \times 10^{-3}$ eV^2 (inverted hierarchy) [4].

While these experiments have succeeded in measuring mass differences between the three eigenstates, the absolute masses of the eigenstates have not yet been measured and cannot be extracted from oscillation experiments alone. Spectrometers have set limits on the effective electron neutrino mass by measuring the endpoint of the β-decay energy spectrum: $\langle m_\beta \rangle = \sqrt{\sum_i m^2_i U^2_{ei}} < 2$ eV [5]. The Planck collaboration has set a limit on the sum of all three neutrino masses $\sum m_\nu < 0.23$ eV using cosmological observations [6].

These limits constrain neutrino masses to be more than five orders of magnitude lighter than the electron, the next lightest particle. If the neutrino interacts with the Higgs field with the same mechanism as the charged fermions, this constrains the couplings to be quite small, six orders of magnitude less than the electron coupling. A

more elegant explanation of neutrino mass comes from adding a non-renormalizable neutrino term to the standard model Lagrangian. In this case, neutrino masses naturally turn out to be much smaller than other fermion masses [7, 3].

This description of neutrinos leads us to the second question: whether or not the neutrino is a Majorana particle. Particles with this property are their own antiparticles. Since the neutrino has zero charge, a Charge-Parity-Time (CPT) mirror image antineutrino will have the same charge as the neutrino; only the helicity will have changed, $\nu_+ \rightarrow \nu_-$, where $\nu_{+(-)}$ represents the positive (negative) neutrino helicity. But the helicity can also be changed by a Lorentz boost. In the Majorana description of neutrinos, a Lorentz boost is equivalent to a CPT mirror operation. If the neutrino is not a Majorana particle (a Dirac particle) there are four helicity-antiparticle combinations: ν_+, ν_-, $\bar{\nu}_+$ and $\bar{\nu}_-$. If the neutrino is a Majorana particle, there are only two states: ν_- and ν_+ [8].

A given neutrino with negative helicity ν_- has a CPT mirror image $\bar{\nu}_+$ (in a CPT invariant theory). If the neutrino is a massive particle, then a Lorentz boost can also be used to change the helicity of the neutrino without changing the charge parity: $\nu_- \rightarrow \nu_+$. As before, the CPT mirror image of ν_+ is $\bar{\nu}_-$. This gives the four assumed states of Dirac neutrinos.

However, if the state ν_+ is identical to $\bar{\nu}_+$, then these states reduce to only two Majorana neutrinos. Either a Lorentz boost or a CPT transformation changes one state to another: $\nu_- \longleftrightarrow \nu_+$. In this case, a CPT transformation only reverses the helicity, unlike in the case of Dirac neutrinos, where antineutrinos are described separately. This is called neutrino-antineutrino duality. This duality exists only for massive neutrinos. As neutrino masses approach zero, the difference between Majorana and Dirac neutrinos becomes less [8].

Given the possibility that the neutrino is a massive Majorana fermion, the question is raised: How can experiments measure this property? The difference between Dirac and Majorana neutrinos diminishes with smaller neutrino masses [8]. Neutrinoless double-beta decay ($0\nu\beta\beta$, described below) can only proceed if neutrinos are Majorana particles. $0\nu\beta\beta$ is not only the most sensitive way to test the Majorana nature of the neutrino but also proceeds at a decay rate related to neutrino mass.

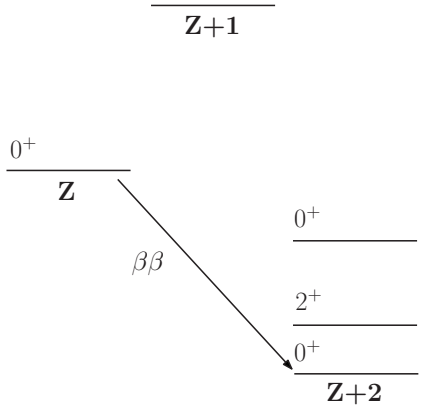

Figure 1.1: Simplified level diagram for a generic double-beta decay. The single β-decay to $Z+1$ is energetically forbidden, allowing the $\beta\beta$ decay to $Z+2$. Decays to the excited states of the $Z+2$ nucleus are also possible $\beta\beta$ decays. From [2].

1.1 Neutrinoless Double-Beta Decay

Neutrinoless double-beta decay ($0\nu\beta\beta$) only proceeds if the neutrino is a Majorana particle [2]. Searches for this decay are the leading technique to determine the Majorana nature of the neutrino. The rate of $0\nu\beta\beta$ is proportional to the absolute neutrino mass, so any measurement of $0\nu\beta\beta$ will depend on the neutrino mass as well. Measurement of $0\nu\beta\beta$ is a possibility in some isotopes for which single β decay is energetically forbidden or highly suppressed by angular momentum. These same isotopes undergo two-neutrino double-beta decay ($2\nu\beta\beta$), which has been measured in several isotopes with half-lives in excess of 10^{18} years [2].

$2\nu\beta\beta$ is a Standard Model process in which two β decays take place simultaneously, only measurable in some even-even nuclei for which β decay is suppressed. Figure 1.1 shows a generic level-diagram of a $\beta\beta$ nucleus candidate. The $2\nu\beta\beta$ is the decay:

$$ {}^{N}_{Z}\mathrm{X} \rightarrow {}^{N}_{Z+2}\mathrm{Y} + 2e^{-} + 2\bar{\nu}_{e}. \tag{1.2} $$

$0\nu\beta\beta$ experiments are searching for the lepton-number violating process:

$$ {}^{N}_{Z}\mathrm{X} \rightarrow {}^{N}_{Z+2}\mathrm{Y} + 2e^{-}. \tag{1.3} $$

In this hypothetical decay, the neutrinos are not emitted, which requires that the neutrino is a Majorana fermion, shown in Figure 1.2. Note that this process changes the lepton number by two units. If the decay proceeds with the exchange of light Majorana neutrinos—the most commonly treated mechanism—the $0\nu\beta\beta$ rate is directly proportional to the square of the effective Majorana neutrino mass, $\langle m_{\beta\beta}\rangle$,

$$\left(T^{0\nu}_{1/2}\right)^{-1} = G^{0\nu} \cdot |M^{0\nu}|^2 \cdot \langle m_{\beta\beta}\rangle^2, \tag{1.4}$$

where $M^{0\nu}$ is a nuclear matrix element, and $G^{0\nu}$ is a known phase-space factor. Calculated values of nuclear matrix elements vary between models used [9, 10, 11, 12]. The range of the calculated nuclear matrix elements imposes a range of values of neutrino masses calculated from a future measured $0\nu\beta\beta$ half-life. $\langle m_{\beta\beta}\rangle$ is a linear combination of mass eigenstates:

$$\langle m_{\beta\beta}\rangle^2 = \left|\sum_i U^2_{ei} m_i\right|^2 . \tag{1.5}$$

Figure 1.3 shows possible values for $\langle m_{\beta\beta}\rangle$ given the lightest neutrino mass $m_{\min}$ in both the inverted (blue) and normal (red) hierarchies. The spaces between the solid lines represent the allowed masses given the best fit values of oscillation parameters from [4]. The space between the dashed lines shows allowed values including 3σ uncertainties.

$0\nu\beta\beta$ experiments probe both the Majorana nature of neutrinos and the absolute scale of the mass. If the neutrino is in fact a Majorana particle, then the decay can proceed and lepton number is violated. If the neutrino is a Dirac particle, the decay will not proceed and it cannot be used to measure the neutrino mass or lepton number violation.

Many experiments have searched for $0\nu\beta\beta$ and set limits on the half-lives of several candidate isotopes. The GERDA collaboration set the half-life limit in ^{76}Ge to be $T^{0\nu}_{1/2} > 2.1 \times 10^{25}$ years [13]. EXO-200 set the limit in ^{136}Xe at $T^{0\nu}_{1/2} > 1.1 \times 10^{25}$ years [14]. KamLAND Zen set a half-life limit in ^{136}Xe at $T^{0\nu}_{1/2} > 1.9 \times 10^{25}$ years [15]. A comparision of half-lives in both elements is shown in Figure 1.4.

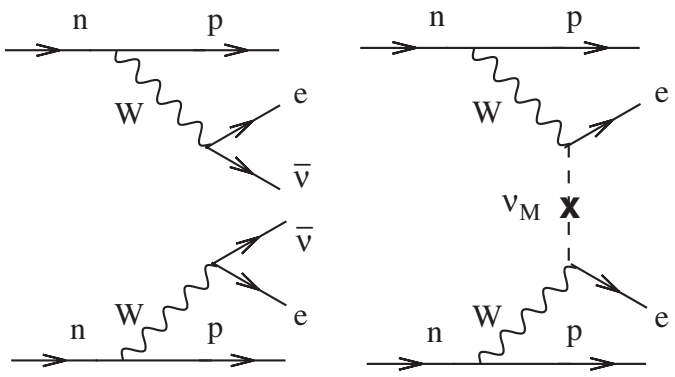

Figure 1.2: Feynman diagrams for two-neutrino double-beta decay (left) and neutrinoless double-beta decay (right). From [2].

One experiment has claimed a detection of the $0\nu\beta\beta$ in ^{76}Ge. Klapdor-Kleingrothaus et al. [16] claim a detection consistent with a Majorana neutrino mass of 0.39 eV [17]. This result is now highly disfavored by recent experiments in ^{136}Xe [14, 15] and ^{76}Ge [13], although this is still being debated [18]. A more complete list of experimental efforts is reviewed in [1].

1.2 The nEXO Experiment

^{136}Xe is an optimal isotope for a $0\nu\beta\beta$ experiment because the beta decay of ^{136}Xe to ^{136}Cs is energetically forbidden. Like EXO-200, nEXO will use ^{136}Xe because it presents a number of advantages over other isotopes.

First, because detection requires a large active mass, isotopes with high natural abundance are preferred. The natural abundance can be augmented by enriching the source material in the $\beta\beta$ isotope. ^{136}Xe can be enriched from the natural abundance of 8.68% to 80% or more with relatively little expense.

Second, γ-rays do not penetrate deeply into Xe because of its high Z. Due to this self-shielding, the center of a monolithic detector will have few γ events, which reduces the primary background to the signal. Despite great effort to purify the material used to construct the detector, there will be some small amount of γ-emitting radiation that could obscure the signal. Since signals near the edge of the detector are more

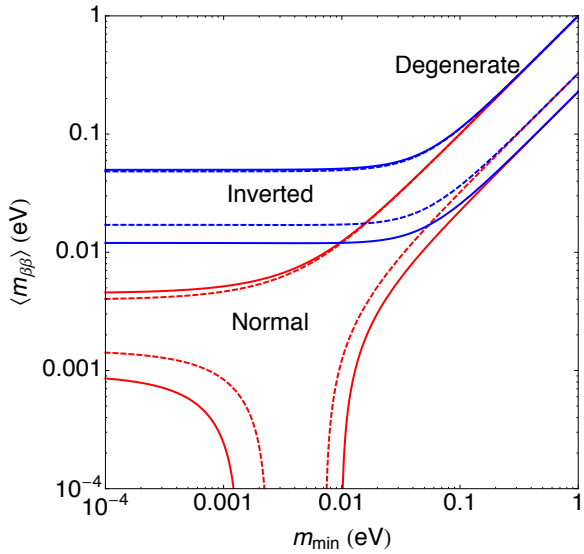

Figure 1.3: The effective Majorana neutrino mass $\langle m_{\beta\beta} \rangle$ as a function of the mass of the lightest neutrino, m_{min}. If the neutrino is a Majorana particle, measurements of the effective Majorana mass $\langle m_{\beta\beta} \rangle$ can help determine if the neutrino hierarchy is inverted or normal. The blue lines outline the inverted hierarchy, while the red lines show the allowed area for the normal hierarchy. The overlap between these two is described as "degenerate." The area between the red (blue) dashed lines shows the allowed area for normal (inverted) hierarchy Majorana neutrinos with variation of the Majorana phases. Parameters from [4].

likely to be γ events while $0\nu\beta\beta$ should occur uniformly throughout the detector, the signal-to-noise ratio can be improved by optimally fitting signals with respect to their position in the detector.

Third, Xe detectors can be purified continuously during operation, which eliminates both radioisotopes in solution and electronegative impurities that capture signal electrons. EXO-200 uses continuous recirculation through getters to eliminate electronegative impurities, ensuring that most electrons produced in events are recorded.

Finally, a Xe detector can allow the removal and identification of the daughter of $0\nu\beta\beta$. A system to further reduce the backgrounds through identification of the decay product, ^{136}Ba, thereby augmenting the background rejection, is under study and is the subject of this thesis. The product is expected to remain a $^{136}Ba^{++}$ ion in the liquid xenon (LXe) detector. LXe detectors allow the decay product to be

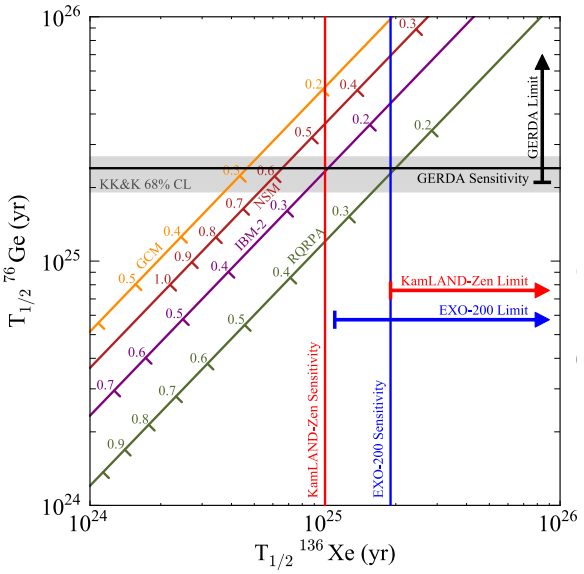

Figure 1.4: A comparison of several theoretical matrix element predictions of $m_{\beta\beta}$ in eV, along with experimental results from ^{76}Ge and ^{136}Xe [14]. Current limits on $0\nu\beta\beta$ in ^{136}Xe are plotted against the x axis, while current limits and the detection in ^{76}Ge are plotted against the y axis. The masses predicted for $m_{\beta\beta}$ in eV are plotted on the diagonal lines. Each line shows the mass predicted by a particular nuclear matrix element theory, including GCM [12], NSM [10], IBM-2 [9], and RQRPA [19].

recovered from the detector medium, but the decay location must be known.

These advantages can be built into a detector that also serves as the source of $\beta\beta$ decays in a tracking calorimeter called a Time-Projection Chamber (TPC) [20]. A TPC detects energy deposits from radioactive decays and other high-energy particles using scintillation light and ionization from the Xe. The scintillation light provides a prompt signal that records the time of the event. Electrons from ionized Xe are drifted to the end of the detector, where charge arrival times and locations in the x-y plane are recorded. From the x-y positions recorded by the ionization electrons and the time elapsed from the prompt scintillation light, the full topology of the event is recorded along with the energy. A full reconstruction of the event topology allows discrimination between α, β and γ events.

The ability of a TPC to track event topology allows the exclusion of most gamma backgrounds that have not been eliminated through shielding from external sources

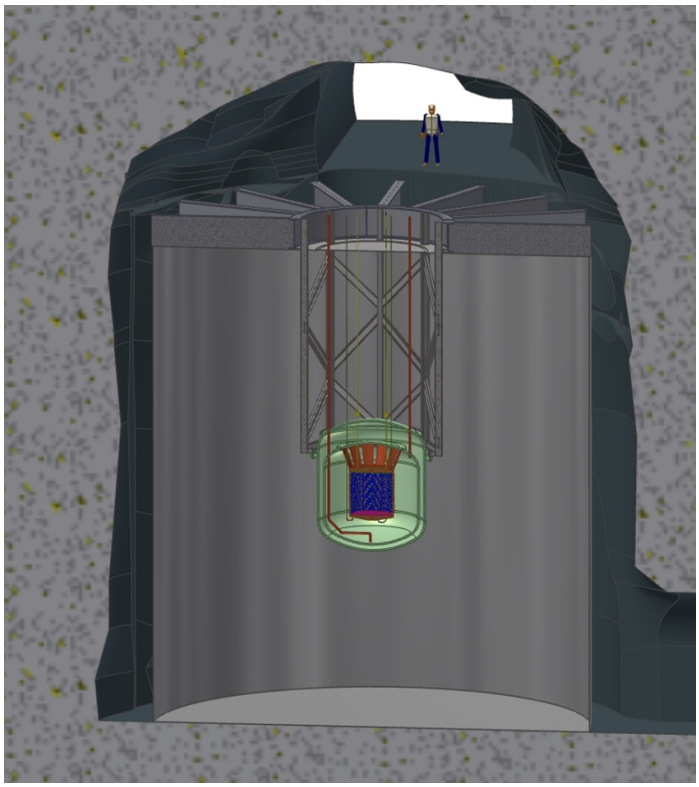

Figure 1.5: The nEXO detector, cryostat, and water muon veto in the SNOLab cryopit.

of radiation and the use of specially selected low radioactivity materials throughout the detector [21]. γ events produce energy deposits at multiple locations through Compton scattering in the liquid xenon (LXe). Since $\beta\beta$ decays deposit the full decay energy in a single location, distinguishing between signal and background is aided by this measurement of event topology.

nEXO has the goal of probing the inverted hierarchy of Majorana neutrino masses (see Fig. 1.3). nEXO will consist of a 5-ton liquid enriched-xenon detector located in the SNOLAB cryopit in Sudbury, Ontario. It is designed to be as similar as possible to EXO-200 to build on the success of that experiment, which first measured the half-life of the $2\nu\beta\beta$ of ^{136}Xe [22, 23], and also set limits on the $0\nu\beta\beta$ decay [14]. A rendering of the experiment is shown in Figure 1.5.

nEXO will take advantage of the same properties of Xe that EXO-200 used, and

it will be upgradeable to allow identification of the ^{136}Ba daughter. Spectroscopic identification of ^{136}Ba from $0\nu\beta\beta$ can eliminate backgrounds due to other radioactive decays. In a normal decay-counting experiment with background that must be subtracted statistically, the sensitivity to the effective mass (Eq. 1.4) scales as the fourth root of the exposure (N source atoms times exposure time t):

$$\langle m_{\beta\beta}\rangle \propto \frac{1}{\sqrt{T_{1/2}^{0\nu\beta\beta}}} \propto \frac{1}{(Nt)^{1/4}}. \tag{1.6}$$

However, if all backgrounds inside the region of interest around the Q value—such as γ events that are not eliminated by topological cuts—can be eliminated, the effective mass scales instead with the square root of the exposure:

$$\langle m_{\beta\beta}\rangle \propto \frac{1}{\sqrt{T_{1/2}^{0\nu\beta\beta}}} \propto \frac{1}{\sqrt{Nt}} \text{ [24]}. \tag{1.7}$$

Once upgraded with a Ba tagging system, the nEXO detector will take advantage of this scaling. It is expected that only 2.5 $2\nu\beta\beta$ events will occur in the 2σ region of interest with an energy resolution of 1%.

The nEXO collaboration is developing several technologies in parallel for detection of the ^{136}Ba daughter. Technologies for extraction in liquid include probes that freeze the Ba^{++} ion in xenon ice on a probe inserted to the site of the decay, then detected using fluorescence spectroscopy in the solid xenon matrix. The probe for this system would have cryogenic cooling as well as optical access to allow for capture and detection of the Ba^{++} ion. A second system seeks to detect Ba^{+} ions desorbed from a surface by thermionic emission. In this case, the Ba^{++} would be adsorbed on a substrate then re-emitted as a singly-charged ion once the substrate is heated.

Future Xe $0\nu\beta\beta$ detectors may use the gas phase of Xe. Gas phase Xe TPCs may have the ability to measure the opening angle between the emitted electrons in $\beta\beta$ events [2]. Technologies to tag Ba from gas are also under development. In gas detectors, the Ba^{++} ion resulting from $0\nu\beta\beta$ is drifted to a nozzle at one end of the detector and passed through several differential pumping stages before the Ba^{++} ion

is extracted into vacuum, where it can be detected using atomic spectroscopy, for instance using a Paul trap [25, 26]. Because the $0\nu\beta\beta$ may produce a Ba^{++} ion, it is possible that such a system will need to convert $Ba^{++} \rightarrow Ba^{+}$.

The 90% CL sensitivities projected for the nEXO program are $T_{1/2}^{0\nu\beta\beta} = 6.0 \times 10^{27}$ years without Ba tagging, and $T_{1/2}^{0\nu\beta\beta} = 3.2 \times 10^{28}$ years with Ba tagging. The sensitivity for these half-lives would extend the reach of the experiment to neutrino masses into the normal hierarchy for all of the common nuclear matrix elements.

This work focuses on the development of a technique to recover the ^{136}Ba resulting from the $\beta\beta$ decay. This technology uses surface adsorption to transport the ^{136}Ba from the TPC, then laser induced thermal desorption and resonance ionization to remove the atom and identify it.

Chapter 2 describes the physics relevant to adsorption and desorption of Ba. The efficiency of this technique relies on a detailed understanding of how Ba adsorbs to substrates. The process of Laser Induced Thermal Desorption (LITD) is also crucial to efficient transfer of ions. The Resonance Ionization Spectroscopy (RIS) process is summarized in Section 2.3.

Chapter 3 addresses the design and construction of a device to test this recovery technique, starting from Ba ions in liquid Xe. This chapter covers both the design and operation aspects of the liquid tagging test device.

Ba recovery results are described in Chapter 4. These results include a description of the signal from various substrates as well as results of deposits in vacuum. The techniques used to clean substrates are described in Chapter 5. These techniques are necessary to ensure that the substrate is free of Ba contamination as well as atoms that could react with Ba.

Finally, because this is an ongoing research and development project, Chapter 6 provides an outlook for the development of the technique in the foreseeable future.

Chapter 2

Laser Induced Thermal Desorption and Resonance Ionization Spectroscopy

The barium tagging technique described here relies on adsorption of the individual Ba^{+} ions onto a substrate from liquid xenon (LXe), desorption into vacuum, and resonant reionization of the Ba atom. Each of these processes must be well understood to maximize the efficiency of recovery—a necessity for an effective barium tagging technique.

In the final application of this technique in a LXe TPC, a substrate is moved to the site of the $0\nu\beta\beta$ decay, then an electric field attracts the Ba^{++} ion and binds it to the substrate. We assume that once the atom is adsorbed to the substrate it acquires electrons from the conduction band of the material[1]. How it binds—and therefore also how easily it desorbs into vacuum—depends on the chemistry between the adsorbate and the substrate atoms. Adsorbed Ba atoms bond with different strengths to different substrates. This interaction can depend upon the atoms in the substrate as well as the structure of those atoms [27].

Laser Induced Thermal Desorption (LITD) removes atoms adsorbed from the

[1]In order to prevent chargeup during laser induced thermal desorption that affects operation of the system, only substrates with finite resistivity are considered in this experiment.

substrate (called *adatoms*) from the substrate using a laser pulse that heats the substrate enough to thermally dissociate the adsorbate-surface bonds. Because LITD pulses are relatively low-energy and in IR wavelengths, the probability of ionizing the desorbed species through direct photoionization or multiphoton ionization is low. Higher-energy laser pulses are known to melt the surface, ionize the desorbed atoms, and ablate large clusters of substrate atoms from the surface [28, 29], which would lead to backgrounds or reduced Ba recovery efficiency.

RIS allows selective and efficient ionization of neutral Ba atoms in the desorbed plume from LITD. These atoms may be the expected Ba signal, substrate atoms and other surface adatoms. Because RIS is so selective, it will ionize only the Ba atoms in the plume. It is also capable of high ionization efficiency, which allows single-atom detection [30].

While ideally LITD should produce neutral Ba atoms that are then ionized by the RIS lasers, thermal desorption processes can remove ionized species from the substrate [31, 32]. These ions produced in LITD could constitute a background to the Ba^+ signal. For this reason, pulses of ions resulting from LITD+RIS can be drifted through a time-of-flight (TOF) mass spectrometer for m/q separation. The resulting m/q spectrum, combined with the selectivity of the RIS process, allows detection of small numbers of Ba^+ ions from other atoms adsorbed to the substrate.

2.1 Adsorption and Thermal Desorption

When an atom bonds to a substrate, the strength of the bond is determined by the chemical interaction between the adsorbate and the substrate. *Physisorption* is an extension of the image charge and other physical mechanisms such as van der Waals forces. Physisorption bond energies are limited to $E_{\text{ads}} < 0.5$ eV. Physisorption is observed in noble gas atoms attaching to surfaces at low temperatures and also in some systems in which it is the precursor to a stronger bond. *Chemisorption* is an extension of chemical bonding to substrates, in which adsorbates form covalent or ionic bonds with energies of $E_{\text{ads}} > 0.5$ eV [27, 33]. Ba is a very reactive atom and bonds tightly to many substrates (such as Si [34], W [35], Ni [36], Ag [37], and

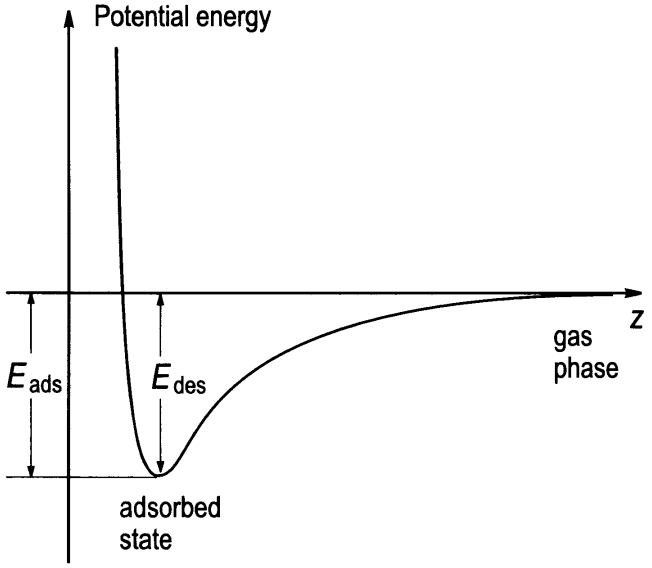

Figure 2.1: The adsorption curve of a generic chemisorbed species. In this case, there is no precursor or barrier to adsorption on the substrate. From [27].

Nb [38]). Because the Ba-substrate bond is strong in these cases, this work focuses on chemisorption.

An example chemisorption potential is illustrated in Figure 2.1. This shows the potential energy of an adsorbate as a function of the distance from the surface z. Atoms incident on the surface may bind to the surface; the fraction of atoms that bond is referred to as the "sticking fraction." In this case, each adatom on the substrate is assumed to stick and bind with an energy E_{ads}, in this case equal to the energy of desorption E_{des}. Note that there is no physisorbed precursor to the adsorption. Ba^+ ions, being quite reactive, should stick well to the substrate. The rate of desorption r_{des} for a single atom can be described by the Arrhenius expression, which describes the temperature T dependent rate for a process with desorption energy E_{des}:

$$r_{\mathrm{des}} = f \exp(-E_{\mathrm{des}}/k_{\mathrm{B}}T). \tag{2.1}$$

The frequency factor f is generally on the order of 10^{12} s^{-1} [27, 39]. k_{B} is Boltzmann's constant. In the limit of small surface coverages, adatoms interact little with each

other, thus E_{des} remains constant. The probability of desorption for a single atom in any given time window is given by multiplying Eq. 2.1 by the surface temperature as a function of time $T(t)$:

$$P_{\mathrm{des}}(E_{\mathrm{des}}) = \int_{t_0}^{t_f} f e^{\frac{-E_{\mathrm{des}}}{k_{\mathrm{B}}T(t)}} dt. \tag{2.2}$$

The surface temperature profile over time can be calculated, as shown in the following section.

Experimental data is the best source for determining surface adsorption energies E_{des}. For thermal desorption processes the commonly used experimental technique consists of steadily increasing the substrate temperature while measuring the pressure of the desorbed species [39]. These measurements, however, may not measure the desorption energy of very small coverages of Ba, making them less useful for this project.

Substrate-adatom bond properties for small coverages of atoms can be calculated through *ab initio* techniques [40], which use a variational approximation to compute the electron density in an assembly of atoms. In surface adsorption calculations, typical computations model an adatom on a small section of substrate that is a few atoms in each dimension. These reveal parameters such as E_{des} and the amount of charge that is transferred from the adatom to the substrate. Examples of these calculations are found for Si [41, 42], graphene [43] and W [44], and may serve as a guide for surface selection and preparation.

2.2 Laser Heating

Optical energy is absorbed by free charges in the substrate which then transfer the heat to lattice vibrations in about 10^{-13} s [45]. This thermalization time separates the effects of nanosecond laser desorption from femtosecond laser desorption—since the thermalization time is much shorter than the laser pulse length, thermal processes dominate over electronic excitations. In this work, we use 7-ns laser pulses at 1064 nm for LITD.

An intense 7-ns infrared laser pulse can heat a substrate from room temperature

to a temperature capable of breaking chemisorption bonds on the substrate [46]. The absorbed power density A due to a laser pulse depends on the optical attenuation length μ in the metal. Less power is absorbed near the surface in materials with larger μ, making smaller μ advantageous for LITD[2]. The absorbed power density deposited at a depth z by a laser pulse with a Gaussian profile in time is:

$$A(z,t) = \mu \frac{E}{\sigma_t \sqrt{2\pi}} e^{-\frac{(t-t_0)^2}{2\sigma_t^2}} e^{-\mu z}. \tag{2.3}$$

t_0 is the time of the peak pulse energy, σ_t is the time width of the Gaussian pulse, and E is the total laser pulse energy. There is relatively little heat flow parallel to the surface, thus the one-dimensional heat equation describes the heat transfer in the material [46]:

$$c_\mathrm{p}\rho \frac{\partial T(z,t)}{\partial t} = \frac{\partial}{\partial z}\left[K \frac{\partial T(z,t)}{\partial z}\right] + A(z,t). \tag{2.4}$$

Where T is the temperature, c_p is the heat capacity, ρ is the density, and K is the thermal conductivity. In this system, the initial temperature is room temperature ($T(t=0) = 300$ K) and the temperature deep in the solid remains unchanged ($T(z \to \infty) = 300$ K). Furthermore, it is assumed that no energy is lost to sublimation of surface atoms or optical re-radiation from the surface, since the pulse energy is 10^7 W/cm^2, while the blackbody radiation due to the elevated surface temperature is at most 10^3 W/cm^2 [45]. While properties such as the heat capacity, thermal conductivity and density change with temperature, this model does not account for these changes as the substrate temperature changes. Finite-element analyses have been performed to show comparable temperature profiles while including both phase changes and temperature variations of substrate properties [28, 29].

Figure 2.2 shows the temperature of a heavily doped Si substrate surface modeled using Equations 2.3 and 2.4. Temperature variation of the optical adsorption coefficient μ is not included in this calculation; instead a constant value appropriate for 1100 K was used [47]. Future treatments of laser heating should include variation of the substrate properties, as done in [48]. The laser pulse profile is shown in red, while

[2]This consideration is secondary to the chemical interaction of the atom with the substrate.

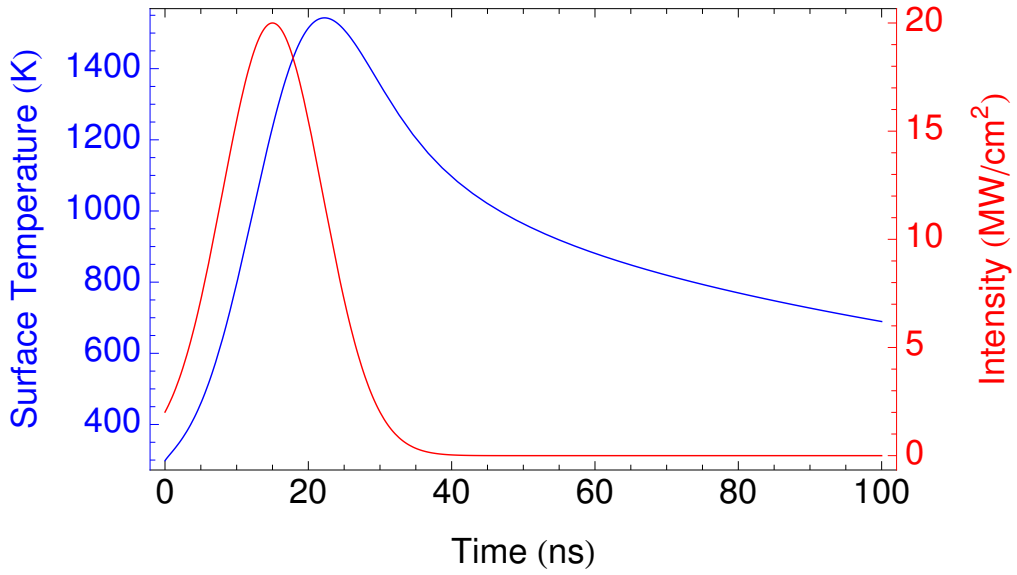

Figure 2.2: Surface heating of heavily doped Si due to a 7-ns Gaussian laser pulse. The maximum laser flux is centered at 15 ns. This was modeled with a numerical solution to Equations 2.4 and 2.3. The temperature does not reach the melting temperature nor the critical temperature of Si.

the surface temperature profile is shown in blue. The surface temperature shown does not exceed the melting temperature of the Si ($T = 1687$ K). The temperature of the substrate can be combined with Equation 2.2 to estimate the probability of desorption in a single laser shot.

This simple treatment of thermal desorption sets limits to acceptable surface bond energies E_{ads} for this application. The bond must be strong enough that the Ba atom does not desorb from the substrate at room temperature over a few minutes, to allow recovery to vacuum. The threshold here is chosen to be a probability of $P = 10^{-4}$. On the other hand, the bond must be weak enough to have a high probability of desorption during several thousand 7 ns laser shots[3], each of which heats the surface

[3]Ideally, there exists a substrate that would allow desorption in many fewer shots.

to 1600 K (an appropriate temperature for LITD from heavily doped Si). In this case the probability of desorption for a single laser shot should be no less than $\sim 10^{-3}$.

A chemisorption bond of $E_{\text{des}} > 1.1$ eV will retain the adsorbate long enough at room temperature to remove the substrate from the detector with $P_{\text{des}} = 1 \times 10^{-4}$. However, a bond of $E_{\text{des}} > 2.2$ eV will effectively keep the Ba from desorbing over thousands of laser shots (here assumed to heat the surface to 1600 K for 7 ns) since in a single laser shot $P_{\text{des}} = 8 \times 10^{-4}$. This sets an approximate range for effective desorption of Ba: 1.1 eV $< E_{\text{des}} <$ 2.2 eV.

If a substrate is found that has $E_{\text{des}} < 1.1$ eV for Ba, the substrate can be cooled to prevent the Ba atom from desorbing. In this case, maintaining the substrate at 170 K will retain an adatom for 1000 s with an adsorption bond as low as 0.6 eV. At the other extreme, substrates with higher melting points, such as Ta or W, can withstand higher temperatures during LITD, allowing values of $E_{\text{des}} < 4$ eV. The selection of substrate for LITD must take into account this competition between thermal desorption due to ambient temperatures and the ability to use LITD to remove atoms from the substrate.

2.3 Resonance Ionization Spectroscopy

After LITD has removed a plume of neutral atoms from the substrate, the Ba atoms must be identified among all desorbed species. Resonance Ionization Spectroscopy (RIS) uses atomic transitions to selectively photoionize Ba from the plume, using pulsed lasers. To be species selective, we use a two-step ionization scheme. These lasers first excite the atom to an atomic resonance, then photoionize it from that resonance. Different spectroscopic combinations can be used to ionize every atomic species in the periodic table [30]. This process applied to ionization of Ba is discussed in more detail in [49].

The simplest RIS scheme uses a single wavelength of light to excite atoms from their ground state into an excited state, from which they are photoionized by a second photon of the same wavelength. This single wavelength is selected to excite the transition from the ground state and to avoid directly photoionizing any other

species that might be present.

This process is selective because it uses the atomic spectroscopy of the targeted atom. For the best selectivity it is necessary to use narrow laser linewidths, so as to avoid exciting other atoms spectroscopically. Processes such as two-photon ionization of other species are highly suppressed because they do not have the resonant enhancement that RIS uses [30].

RIS can approach 100% efficiency with laser intensities adjusted to saturate the transitions, allowing detection of single atoms [30]. The intensity required to saturate an atomic transition can be calculated from laser saturation equations [50].

The Ba tagging system described in this work uses light of two wavelengths: 553.5 nm and 389.6 nm (wavelengths in air). The scheme used is shown in Figure 2.3. 553.5 nm light excites the atoms from the $6s^2\ {}^1S_0$ ground state into the 6s6p $^1P_1$ excited state. The 389.6 nm light excites atoms from the 6s6p $^1P_1$ state to the 5d8d autoionized state. This system of transitions has relatively high cross sections compared to other transitions available in the neutral Ba spectroscopy. The 553.5 nm transition has the highest cross section of all transitions from the neutral Ba ground state [51]. Autoionized states appear in multi-electron atoms in which discrete states interfere with continuum states, leading to transitions that result in ionization of the atom [52]. The use of the autoionized state in the photoionization scheme aids ionization of the Ba atoms by using the relatively high cross section of the state to aid in ionization. The 389.6 nm transition has the highest cross section from the 6s6p $^1P_1$ state among autoionized states in Ba [53]. The high cross section saturates these transitions with modest laser intensities available with commercial dye lasers, which guarantees high-efficiency ionization of the Ba atoms desorbed from the substrate.

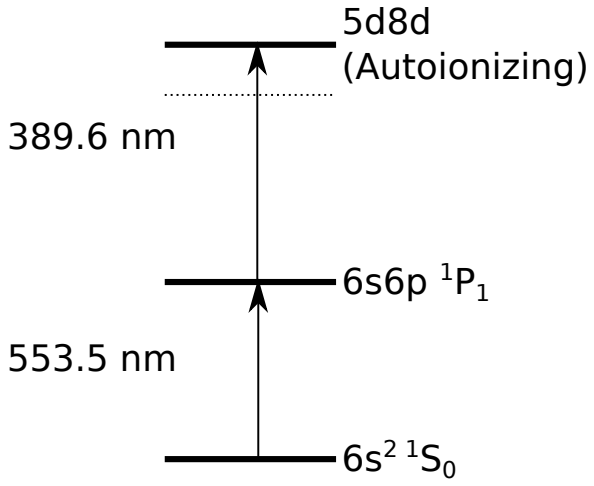

Figure 2.3: The Ba tagging RIS scheme used in this thesis. The dashed line indicates the approximate energy of the first ionization threshold. Wavelengths listed are in air.

Chapter 3

Experimental Apparatus

This chapter describes a system (shown in Figure 3.1) which is capable of testing extraction and identification of Ba^+ ions intentionally deposited in LXe. The approach is to electrostatically drift Ba^+ ions to a clean substrate, adsorb them, then transport the substrate to vacuum with the Ba attached. Neutral Ba atoms are then removed from the substrate using LITD, resulting in a plume of individual atoms in vacuum, making their atomic spectroscopy available for identification. RIS is then used to ionize Ba in the desorbed plume of neutral atoms. This highly selective process allows Ba to be identified despite the possible presence of other elements. RIS is potentially very efficient, thus making the detection of single Ba atoms possible [30].

In order to model and test the final application, the development of this process must use very small numbers of Ba atoms. Removal of Ba from the substrate leads to elimination of the signal, making this measurement intrinsically destructive. Therefore careful control over all aspects of the system is necessary for effective operation.

To positively identify the signal, a time-of-flight (TOF) spectrometer separates Ba ions from other species that are ionized due to various undesirable effects. This extra selectivity complements and cross-checks that of the RIS process. In order to maximize the recovery of Ba, the TOF spectrometer is optimized for ion transport efficiency. The TOF of each ion detected is recorded for later analysis.

In the apparatus, Ba ions can be produced by one of two sources using radioactive decays; one is driven by the recoils of an α decay [54] (appropriate for initial tests in

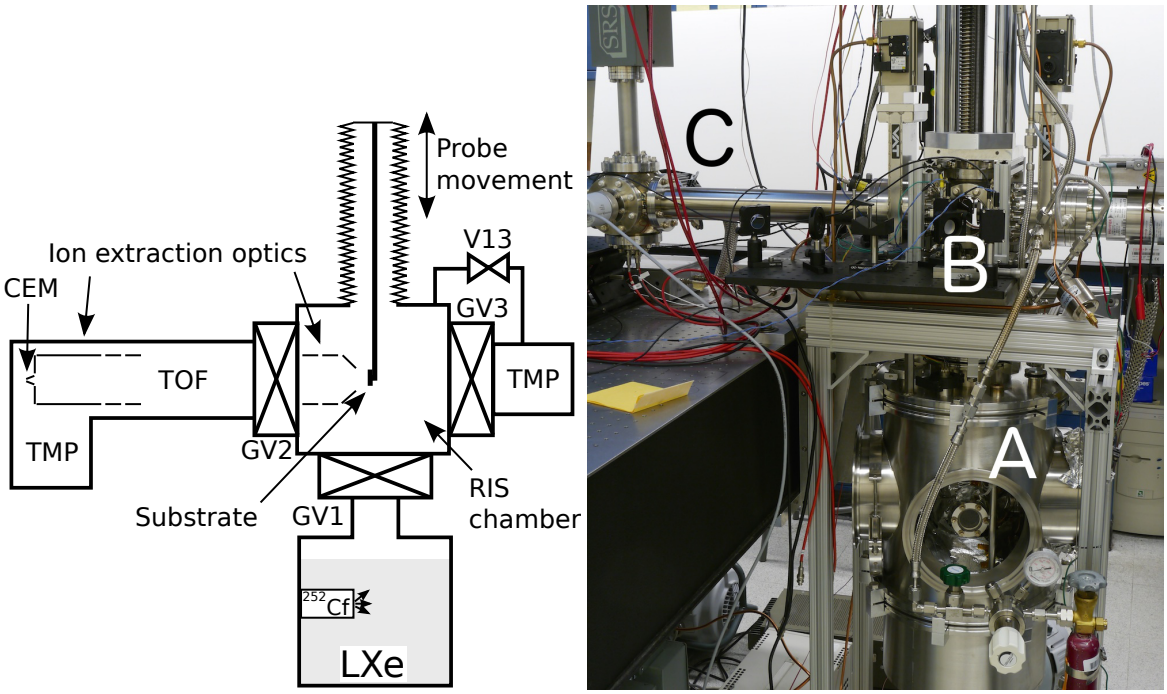

Figure 3.1: Functional diagram (left) and photograph (right) of the Ba tagging system. In the photograph **A** is the LXe cell, **B** is the RIS chamber, and **C** is the TOF spectrometer. Much of the Xe handling system is omitted for simplicity (see Fig. 3.3).

vacuum), while the other is a ^{252}Cf fission source that produces Ba ions directly (to be used for tests in liquid xenon), similar to radioactive beam sources [55]. Because these sources produce Ba ions at a fixed location, there is no need to search the entire LXe volume. Mechanical systems to position a probe at any location within a large LXe TPC will be developed separately for nEXO.

The function of the apparatus shown above in Figure 3.1 can be summarized as follows: The substrate mounted on the end of the probe is lowered into the LXe where the source deposits Ba^+ ions. The substrate is then moved to the RIS chamber, and the gate valve (GV1) is closed to isolate the RIS chamber from the LXe cell. The RIS chamber is evacuated by a combination of cryopumping and the turbomolecular pump (TMP) through GV3, and finally GV2 is opened to the TOF spectrometer for identification of atoms desorbed and re-ionized.

The LXe conditions of this apparatus are similar to those of a LXe TPC: 900 Torr

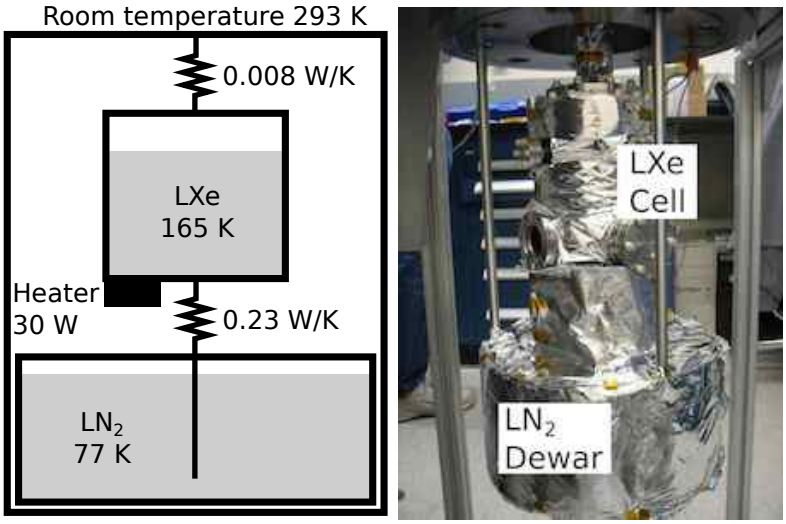

Figure 3.2: Thermal model of the LXe cell and LN_2 reservoir (left) and a photograph (right). The LXe cell is cooled by LN_2 held in a dewar mounted inside the same vacuum insulation. The photograph shows the LN_2 dewar and LXe cell wrapped in super insulation.

pressure at a temperature of 165 K. The apparatus includes systems to cool and condense LXe, and can test Ba tagging from Ba production through retrieval and identification. The following sections describe the function of each subsystem of the apparatus in more detail.

3.1 Liquid xenon cell and probe

This system condenses xenon in a 1 liter copper cell cooled using liquid nitrogen (LN_2). The cell is insulated from room temperature by a vacuum of 10^{-5} Torr. Radiative heating across the vacuum is limited by 10 layers of super insulation.

The 10 liter LN_2 dewar is mounted in the same vacuum as the LXe cell, as shown in Figure 3.2. The cell is connected to the LN_2 bath through a copper heat-transfer strap. Because the thermal conductivity of this strap is much greater than the thermal conductivity of the tube leading to room temperature, the equilibrium temperature is below the temperature required to maintain the Xe in liquid phase (165 K), typically requiring about 20 W of heating power. The heaters are controlled through a PID

loop using the cell temperature measured by Resistive Thermal Devices (RTDs) read out by a PLC system[1]. To ensure thermal stability and uniformity, the LXe cell is built with 1.9 cm thick copper walls.

Access to the cell is provided through several CF flanges brazed into the copper cell body. The cell is supported from the top CF 6.00" flange, through which the probe passes. Eight CF flanges (4× CF 2.75", 4× CF 1.33") are available to mount viewports, sources, and voltage feedthroughs. The Ba source is mounted on one of these CF 2.75" ports, while the other three are reserved for optical access to the LXe (Labeled A in Figure 3.1).

3.1.1 Xenon delivery and recovery

A schematic view of the vacuum and Xe systems is shown in Figure 3.3. Since the measurement requires shuttling the probe between the LXe ($\sim$ 900 Torr) and the TOF spectrometer (vacuum), the RIS chamber functions as a load-lock isolated by three gate valves (Fig. 3.1). The LXe level must be maintained while GV1 is closed, which requires xenon feed to and recovery from the cell. At the same time, xenon must be added to or removed from the RIS chamber either to pump the RIS chamber to vacuum or to balance the pressure across GV1 before opening it. Xenon feed to and cryopumping from both the cell and the RIS chamber are controlled by pneumatically-actuated valves (V9-V12).

Xenon is supplied to the system from a two-bottle manifold: one serves as the supply, the other serves as a recovery/cryopump bottle. For any given run, the manual valves are configured to feed xenon from the supply bottle through the regulator and purifier[2] to fill the cell. The recovery bottle is empty at the beginning of a measurement cycle and is immersed in LN_2. At the end of a run all of the xenon is transferred to the recovery bottle. The recovery bottle is then warmed up and serves as the supply bottle for the next run. Bottle manifold valves (V1-V6), V7 and V8 are manual.

[1]National Instruments Ethernet RIO NI-9148.
[2]SAES Pure Gas, Inc. model HP400-903F.

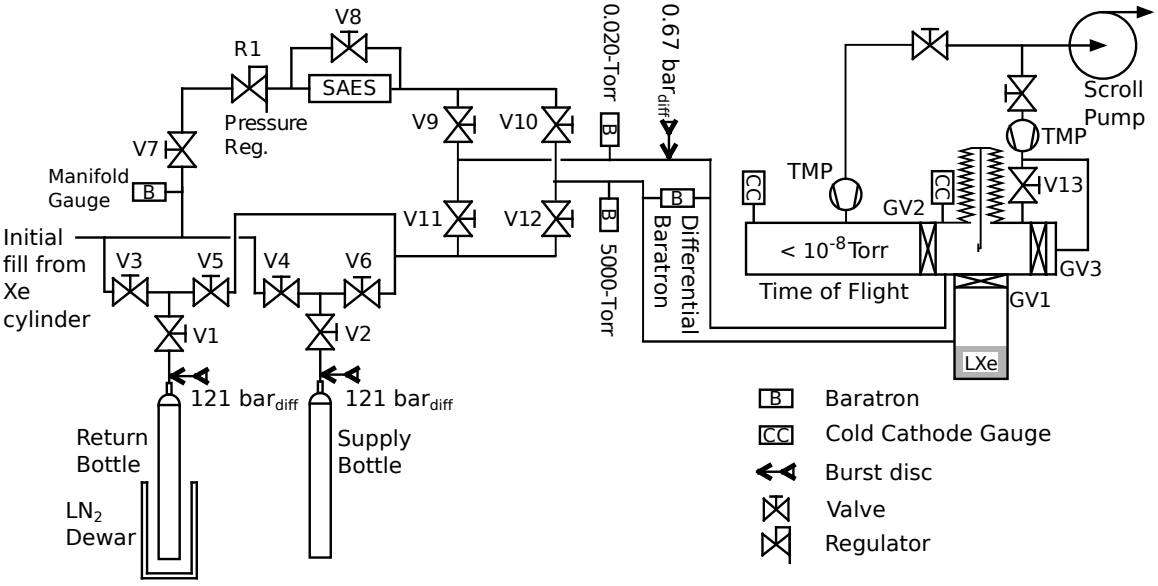

Figure 3.3: Vacuum and xenon systems. Valves are configurable to feed xenon from either bottle, and recover it to the other, immersed in LN_2. Valves allow feeding and recovering LXe from both the LXe cell and the RIS chamber, which allows sampling the substrate in vacuum while maintaining the LXe in the cell. Turbomolecular pumps (TMP) maintain the TOF at UHV and are used to bring the RIS chamber to vacuum.

Capacitance manometers measure pressure throughout the xenon system. Pressure in the LXe cell is measured by a 5000-Torr full-scale gauge, while pressure in the RIS chamber is measured by a 20-mTorr full-scale gauge[3]. Pressure across GV1 is measured by a differential Baratron[4]. Vacuum is measured with cold cathode gauges[5] on the RIS chamber and the TOF spectrometer.

All temperatures and pressures are recorded at a 1 Hz rate and serve as input to a PID loop that controls valve states and the two 30 W resistors that are used to heat the LXe cell. Pneumatic valves (V9-V13 in Figure 3.3) are controlled by a digital output to add or remove xenon from the system. The gate valves (GV1-GV3 in Figures 3.1 and 3.3) are also controlled by the PLC system.

The Ba collection cycle begins with all three gate valves (GV1-3) closed, with the RIS chamber under vacuum. GV1 can only be opened after the Xe pressure across it has been balanced by filling the RIS chamber through V9. The probe can then move the substrate into the LXe. Once Ba has been deposited and the substrate has been retracted to the RIS chamber, the system is configured to recover the Ba: GV1 is closed, the RIS chamber pumped to vacuum. Cryopumping to the recovery bottle reduces the pressure in the RIS chamber from ~ 900 Torr to less than 1 Torr in ~ 1 minute. A high-impedance bypass valve (V13) opens to bring the pressure to below 10^{-3} Torr with the turbomolecular pump always running at full speed. GV3 then opens when the RIS chamber is at 10^{-3} Torr and finally GV2 opens with the RIS chamber pressure below 10^{-5} Torr. This procedure loses roughly 0.02 g of Xe by pumping it into the atmosphere.

3.2 Barium ion sources

A Ba^+ ion source is necessary to produce the small amount of Ba needed to develop this technique. For some tests the Ba^+ has to be produced in LXe, adding special constraints because of its high density. Sources producing large and hard to control

[3]MKS Baratrons, part numbers 627D53TBC1B and 627DU2TBE1B.
[4]MKS Baratron, Part Number 226A13TCDCDFB2A1.
[5]Pfeiffer Vacuum Full Range Gauges.

Isotope	Half-life	SF fraction
^{238}U	4.47×10^9 a	5.5×10^{-5}
^{244}Cm	18.1 a	1.4×10^{-4}
^{246}Cm	4.76×10^3 a	0.03%
^{248}Cm	3.48×10^5 a	8.39%
^{250}Cm	8.3×10^3 a	74%
^{250}Cf	13.1 a	0.08%
^{252}Cf	2.646 a	3.09%

Table 3.1: An abbreviated list of spontaneous fission isotopes. These are the isotopes considered as sources of Ba^+ ions in LXe. Medium-long half-lives provide consistent amounts of Ba over long periods of time with minimal source atoms. High spontaneous fission fractions ensure that most of the decays go toward the fission products, including Ba.

quantities of Ba were not considered. Currently, a Gd-driven Ba ion source is used in vacuum; the use of a fission source is planned for LXe. In the Gd-driven source, recoiling nuclei from the α decay of ^{148}Gd sputter Ba and BaF atoms and ions from the BaF_2 layer. Most atoms are emitted with energies under 1 keV, but the energy distribution has a long tail extending to 89 keV. This source has been described in a separate publication [54].

Because the Gd-driven source produces ions at a very low energy, the ion range is very short in LXe. We plan to produce Ba ions in LXe using a ^{252}Cf source[6], electroplated on Pt in such a way as to allow the fission fragments to escape. Each fission produces two neutron-rich isotopes, which β decay to stable isotopes. Ba isotopes are produced by the fission products and subsequent decay chains of ^{252}Cf. The energy of fission fragments averages around 70 MeV, enough to deliver the Ba ~ 30 μm into the LXe, calculated using SRIM [56].

There are a number of isotopes with masses around 250 amu that spontaneously fission, where the heavier fission product distribution is centered around 140 amu, making it a good candidate for producing Ba isotopes through β-decay. Table 3.1 shows a list of the isotopes considered.

Half-life is the first consideration. In order to deliver a consistent amount of

[6]Isotope Products, Valencia, CA.

Ba over the course of the experiment, a longer half-life ensures that the number of decays does not change drastically over the lifetime of the experiment. If a longer-lived isotope were used, it would require a thicker layer, potentially blocking fission fragments from exiting the source. Because of this, the only reasonable half-lives are on the order of a few years.

The second consideration is the fraction of decays that are spontaneous fission, which should be as high as possible. The isotopes with the highest fraction are ^{250}Cm, with a very long half-life, and ^{254}Cf, with a rather short half-life. ^{252}Cf sources strike a medium between these two considerations, and are readily available. The spontaneous fission fraction of ^{252}Cf is 3.09%, while the remainder are α decays. The daughters of this fission process include many isotopes around 140 amu which beta decay through Ba isotopes [57, 58].

Since the fission fractions and decay rates are well known, it is possible to predict the number of each isotope given a probe exposure time. The population of a given Ba isotope is given by the following system of differential equations:

$$\begin{aligned}
\dot{N}_{^{A}Ba}(t) &= N_0\lambda_0 Y^{\text{ind}}_{^{A}Ba} + N_{^{A}Cs}(t)\lambda_{^{A}Cs} - N_{^{A}Ba}(t)\lambda_{^{A}Ba} \\
\dot{N}_{^{A}Cs}(t) &= N_0\lambda_0 Y^{\text{ind}}_{^{A}Cs} + N_{^{A}Xe}(t)\lambda_{^{A}Xe} - N_{^{A}Cs}(t)\lambda_{^{A}Ba} \\
&\vdots
\end{aligned}$$

Where $N_{^{A}Ba}$ is the number of Ba (Cs, Xe, ...) atoms with A equal to the mass number. N_0 is the number of ^{252}Cf atoms decaying at a rate λ_0, and $Y^{\text{ind}}_{^{A}Ba}$ is the independent fission yield for the given isotope. λ represents the decay rate for each isotope, as labeled. The system of equations continues to the most neutron heavy isotopes for each value of A.

The solution of this system of equations leads to a gradual increase for some isotopes fed by longer half-lives (Figure 3.4). Each isotope accumulates atoms from the spontaneous fission yield and β decays, and all but ^{138}Ba β decay to La isotopes. The only stable isotope shown is ^{138}Ba, although there is significantly more ^{140}Ba, which has a half-life of 12.75 days that should be detectable with this technique.

The accumulation of Ba in the LXe from a 1 kBq source is calculated from the

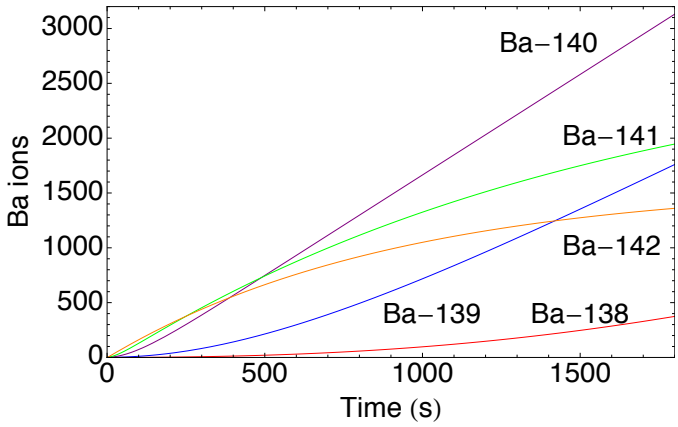

Figure 3.4: The accumulation of longer-lived Ba isotopes created by ^{252}Cf fission. Table 3.2 shows a complete list of half-lives.

Isotope	Half-life	Accumulation after 30 min
^{138}Ba	Stable	375
^{139}Ba	83.1 m	1760
^{140}Ba	12.8 d	3130
^{141}Ba	18.3 m	1950
^{142}Ba	10.6 m	1360

Table 3.2: Isotopes of Ba emitted in large numbers from the ^{252}Cf source.

known fission yields [58] and shown in Table 3.2. This analysis assumes that there are no fission products in the LXe at the start of deposition. Deposition begins when the substrate is moved in front of the source and is biased to attract ions. The source will be biased to readsorb ions resulting from fissions while the substrate is not positioned in front of the source.

The Ba isotopes are primarily produced by β decays from Cs isotopes. ^{134}Ba through ^{137}Ba are not produced in large numbers because the corresponding Cs isotopes are long lived. Heavier isotopes (^{143}Ba and heavier) are too short-lived to be of use in this system [57, 58]. For ^{138}Ba, the only stable isotope produced in a significant amount, the source will produce 375 ions in the first 30 minutes. Other isotopes, such as ^{139}Ba through ^{142}Ba, are relatively long-lived, and will be detectable in this system.

3.3 Laser Setup

Laser induced thermal desorption (LITD) is a convenient method for removing a few atoms from a substrate [46]. Ba is then selectively ionized from the desorbed plume of neutral atoms using RIS. In order to allow the desorbed plume of atoms to move away from the substrate and mitigate image-charge effects, the RIS lasers are delayed by 1 μs with respect to the LITD pulse.

In addition to desorbing neutral atoms, LITD can directly produce ions which are a background to the Ba signal. In order to characterize the various backgrounds during data collection, the LITD and RIS laser pulses are cyclically suppressed. The following three states are alternated:

- Both LITD and RIS pulses (with a 1 μs delay) are retained. Ba is ionized selectively, along with possible backgrounds due to the LITD laser alone.
- Only the LITD pulses are retained. Ions directly generated by the desorption laser alone can be identified and subtracted from the data in the first cycle.
- Only the RIS pulses are retained. This configuration can be used to measure the background that may be produced if the RIS pulses are not properly shaped in space and desorb ions from the substrate.

All lasers fire at a rate of 10 Hz and a system of mechanical shutters implements the pulse sequence described above. This arrangement provides better stability in the pulse energy as the lasers operate in a thermal steady state.

Figure 3.5 provides a simplified schematic of the optical setup. The pulse energy of the desorption laser (1064 nm) is measured by two infrared photodiodes (IRPD1 and IRPD2 before and after hitting the substrate, respectively). Dye lasers pumped by a second Nd:YAG provide the RIS pulses. Both ionization lasers use energy control through $\lambda/2$ waveplates and polarizing beam splitting cubes (BS), and each is measured by a photodiode (GrnPD and UVPD).

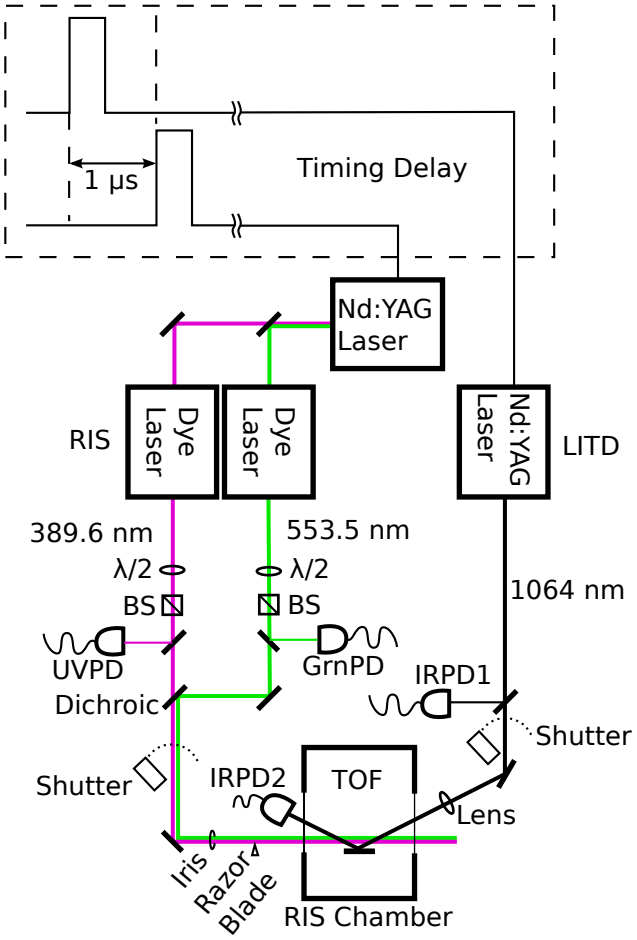

Figure 3.5: Laser optics and timing.

3.3.1 Laser Induced Thermal Desorption

The Ba atoms must be desorbed to form a plume that can be ionized using pulsed dye lasers. We use a pulsed 1064 nm Nd:YAG laser[7] to thermally desorb atoms from the substrate.

The Nd:YAG laser produces a Gaussian beam profile, which is loosely focused onto the substrate using a 200 mm focal length lens. Because of the 70 degree angle of incidence, this results in an elliptical Gaussian profile measuring 275 μm × 750 μm (Gaussian σ) on the substrate. The LITD intensity is typically 2 MW/cm^2 at the center of the spot averaged over the 7-ns laser pulse. The LITD laser spot can be rastered across the substrate to measure spatial variation across the target. Linear stages control the x and y position of the LITD laser spot on the substrate. Upon mounting each target, the LITD laser is scanned across the target to locate the target edges and measure the laser spot size through the reflected power on IRPD2.

The desorption laser pulse energy is carefully controlled to limit ionization from the desorption process. This is done through a built-in waveplate-polarizing beam splitter combination that allows manual adjustment of the laser pulse energy. Individual pulses of the desorption laser are measured by two separate photodiodes[8]. The first infrared photodiode (IRPD1 in Fig. 3.5) measures each individual IR pulse before the beam enters the RIS chamber. Measurement of the reflected beam off of the substrate (IRPD2) is used to aid in positioning the laser spot on the substrate. Both diode readings are recorded for each laser pulse and are calibrated to a powermeter[9].

The desorption laser power must be set to minimize backgrounds but ensure desorption of neutral Ba from the surface. The desorption laser pulse energy is increased until the RIS Ba peak appears indicating that Ba has been desorbed as a neutral atom and resonantly ionized. If the desorption laser produces significant backgrounds at the TOF of Ba, then the pulse energy is reduced.

[7]Minilite II, Continuum Lasers, 7 ns pulse width.
[8]Thorlabs model FDS1010.
[9]Newport Power Meter Model 818P-001-12.

3.3.2 Resonance Ionization Spectroscopy lasers

Tunable dye lasers are used for the RIS process. These lasers are pumped by the second and third harmonics of a separate Nd:YAG laser[10]. The RIS scheme, shown in Figure 2.3, uses two wavelengths [59, 60]: 553.5 nm[11] and 389.6 nm[12]. Both wavelengths are periodically verified using a wavemeter[13] to ensure stability.

The RIS process requires that both RIS beams are spatially and temporally overlapped. Spatial overlap is achieved by using a dichroic mirror that transmits UV light and reflects green light, as shown in Figure 3.5. A razor blade clips the beam profile and an iris blocks the tails of the Gaussian beam obtaining a 5 mm-diameter semicircular beam profile that optimally overlaps the desorbed plume of atoms and grazes the substrate without striking it. This profile overlaps most desorbed atoms from the typical 4 mm $\times$ 4 mm scan of the LITD laser.

Tracking the energies of the laser pulses is crucial to ensure efficient RIS. In particular, the pulse energies of the dye lasers decrease in intensity over time as the dye is bleached. Each laser uses a separate photodiode pickoff to provide a relative energy measurement on a pulse-by-pulse basis. A separate calibration provides the pulse energy at the window to the vacuum chamber. All photodiodes are read out by Flash Analog to Digital Converters (FADCs)[14]. Adjustments to the pulse energy of each laser are made by rotating a $\lambda/2$ waveplate in front of a polarizing beam splitter.

3.4 Time of flight spectrometer

A time-of-flight (TOF) spectrometer (shown schematically in Figure 3.6) allows for mass analysis of the ionic species produced in LITD and RIS processes. As mentioned, non-Ba ions are produced by desorption from the substrate due to the LITD pulse, improperly shaped RIS pulses scraping the surface, non-resonant multi-photon processes and, in the case of the semiconducting substrate mounting technique, the

[10]Spectra Physics INDI-HG.
[11]Sirah Cobra Stretch, using Pyrromethene 580 dye.
[12]Sirah Cobra Stretch with a mixture of Exalite 389 and Exalite 398 dye.
[13]Angstrom HighFinesse.
[14]National Instruments PXI-5105

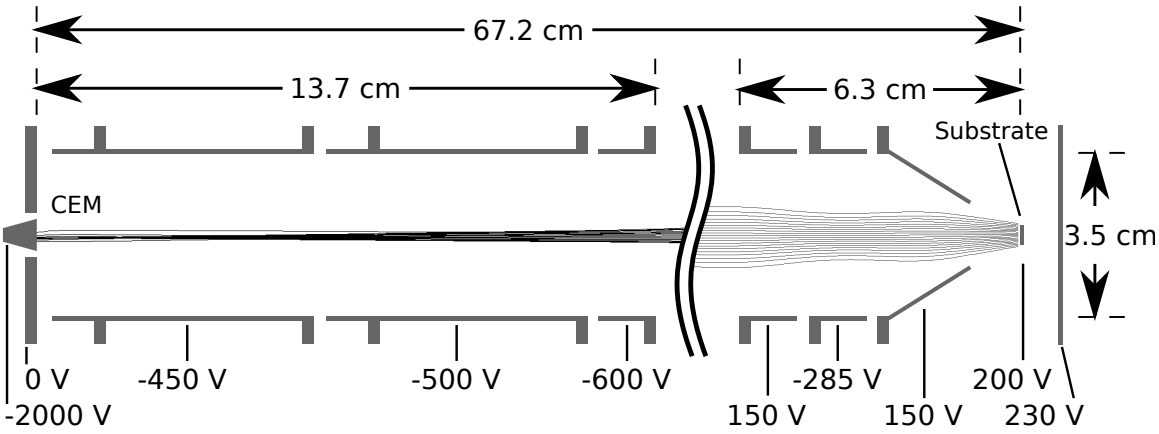

Figure 3.6: The ion optics of the TOF. Ion flight paths simulated using SIMION are shown, in this case starting from a uniform distribution of ions with zero initial kinetic energy. The ion flight paths are focused toward the CEM, accounting for the tighter beam at the detection end.

Mo or Ta clips which may have a lower threshold for removal of ions. A mass resolution on the order of $m/\Delta m \approx 100$ is sufficient to discriminate between the species of interest. It is crucial that the ion transport efficiency of the TOF be very high to allow efficient Ba recovery.

To achieve this, ions are accelerated into the TOF by an electric field of ~ 60 V/cm. The first electrode in the TOF spectrometer is cone-shaped to allow for optical access while maintaining a strong electric field near the substrate. Once the ions have been accelerated into the first lens triplet, they are collimated and drift through the vacuum tube. At the end of the TOF path, ions are focused onto the 1 cm diameter aperture of a channel electron multiplier (CEM)[15] by a second lens triplet. SIMION [61] simulations show a transport efficiency of $> 99\%$ for ions from a thermal distribution appropriate for Ba desorbed as a neutral atom then ionized by the RIS process.

3.5 Substrate Mounting

The substrate must be positioned precisely in both the LXe cell and in the RIS chamber to ensure consistent deposition of Ba and laser desorption. The substrate

[15]DeTech model 2405.

is mounted on the end of a 12.7 mm-diameter, 85 cm long thin-walled stainless steel tube. The vertical probe movement is actuated through a long bellows by a stepper motor outside the vacuum with a nominal vertical position accuracy of 3 μm. Horizontal positioning is guaranteed by pairs of spring-loaded Vespel[16] rollers that constrain the transverse motion of the probe and progressively engage the probe tube as it is lowered into the system.

Substrates are mounted using two different methods depending upon the material. The mounting system must not have protrusions that could adversely affect the electrostatics both for depositing Ba on the substrate and for the RIS process and also minimize the exposure of extraneous parts to the lasers impinging on the substrate. The cleanliness of the substrate is ensured by *in situ* cleaning systems, described in Chapter 5. For resistive heating and electron gun heating, substrate temperatures were measured using a fiberoptic pyrometer[17]. Bias voltages are applied through wiring running down the probe tube.

Metallic substrates are held by a stainless steel clip (Figure 3.7A), insulated from the surrounding stainless steel support by a MACOR[18] insulator. Silicon and silicon carbide substrates are held by Mo or Ta clips in turn supported by a MACOR support (Figure 3.7B). The clips serve as electrical contacts for resistive heating of the substrate for cleaning purposes, described further in Section 5.2.

3.6 Data Acquisition

Data acquisition from the TOF and laser systems is separate from the slow control system that regulates the LXe temperatures and pressures and actuates the probe. TOF and laser data must be recorded at 10 Hz and with sufficient bandwidth to separate pulses from multiple ions within each shot. For each laser shot, a 250 MS/s FADC[19] records data for 60 μs after the RIS laser pulse, long enough to record ions up to 300 amu/e. The CEM produces fast pulses amplified by a high-bandwidth

[16]Vespel is a trademark of DuPont.
[17]Omega model iR2P-600-53-C4EI.
[18]MACOR is a trademark of Corning, Inc.
[19]National Instruments PXI-5114.

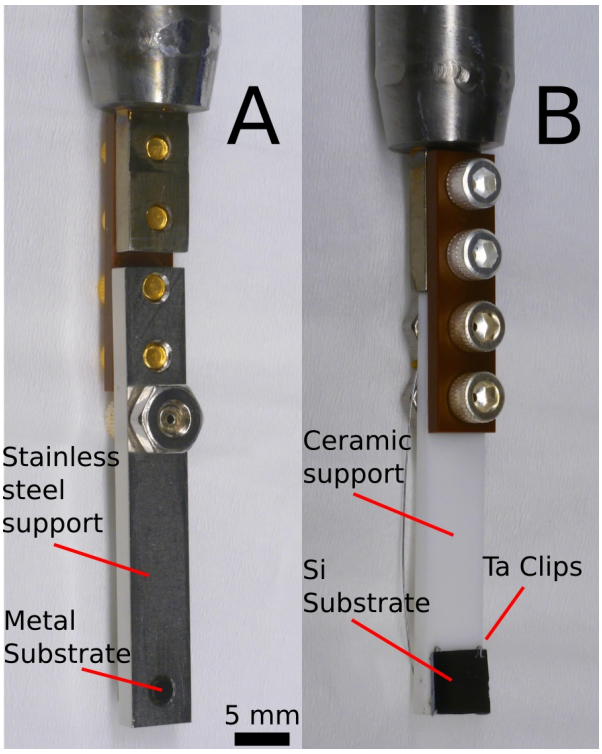

Figure 3.7: Two substrate mounting systems: for refractory metal substrates (A) and for Si and other semiconductors (B). The refractory metal substrate in A is held from behind by a stainless steel clip. The substrate is isolated from the front plate. The Si substrate in B is held by Mo or Ta wire clips.

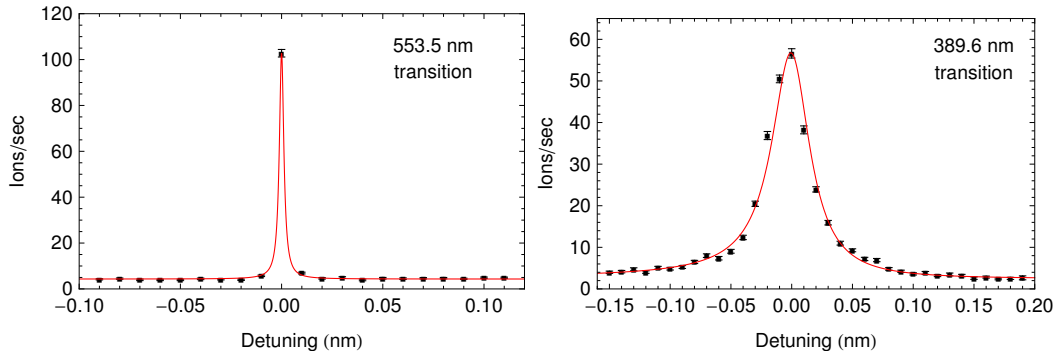

Figure 3.8: Ba^+ rates obtained by detuning the RIS lasers. The left panel shows the 553.5 nm transition, the right shows the 389.6 nm transition. A Lorentzian is fit to the 553.5 nm transition data. A Fano profile (which accounts for interference between the atomic state and the continuum) is fit to the 389.6 nm transition. Power and Doppler broadening are limited. Errors shown are statistical.

preamp[20]. The same data acquisition system records the photodiode readings using 60 MS/s FADCs[21]. A LabVIEW program controls the shutters and a stage that can raster the desorption laser across the substrate.

3.7 Basic Spectroscopy

Efficient RIS requires that the atomic transitions be saturated. Before designing the present system, saturation conditions for both lasers were checked in a separate setup, using an atomic Ba beam. This beam, produced by heating a Ba-coated tungsten wire inside a small volume with an aperture, emitted neutral Ba atoms at a far higher flux than the thermal desorption process described in Sec. 3.3.1, simplifying the spectroscopy measurements.

The two RIS lasers were detuned in turn to obtain the spectra in Figure 3.8. While scanning the 553.5 nm laser, the 389.6 nm laser power was maintained at 140 μJ/pulse with the laser on resonance. The scanning 553.5 nm laser was kept at 100 nJ/pulse and the resulting curve was fit to a Lorentzian curve ($\chi^2/ndf = 38/17$). Errors on the data are statistical-only, possibly leading to large χ^2/ndf values. The 389.6 nm laser

[20]Ortec VT120.
[21]National Instruments PXI-5105.

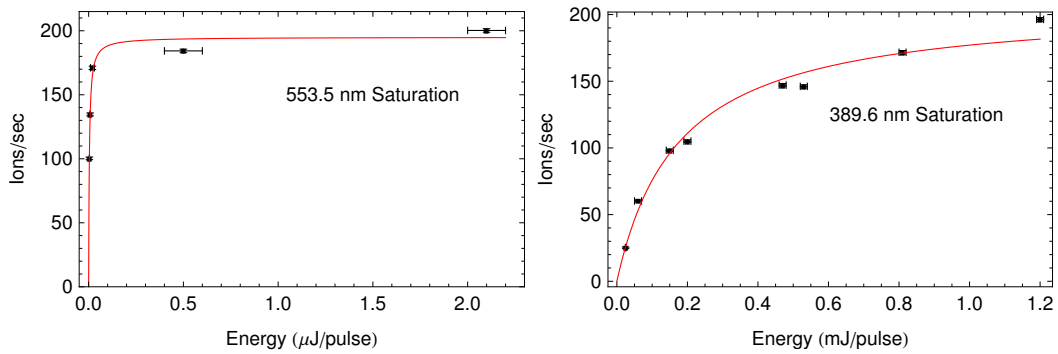

Figure 3.9: Saturation curves for the RIS lasers. The saturation curves do not fit exactly because the saturation curve assumes a uniform laser profile and does not account for the ionization in the tails of the Gaussian beam. These data were produced with a 2 mm σ Gaussian beam. Errors shown are statistical.

was detuned while maintaining the 553.5 nm laser on resonance at 2.3 mJ/pulse. The lineshape of this transition to an autoionizing state is described by a Fano profile [52], which accounts for the interference between the atomic state and the continuum. In this case, $\chi^2/ndf = 194/30$ (still using statistical errors only).

Saturation curves are then obtained with both lasers on resonance while scanning the energy of each laser separately, as shown in Figure 3.9. The data are fit reasonably well by the model in reference [50], although χ^2/ndf values are large, presumably because systematic uncertainties are not taken into account.

3.7.1 Time-of-flight spectrometer calibration

Calibration of the TOF spectrometer is necessary for effective identification of Ba. Since several masses are required, ions generated in the LITD process are used. From such a calibration, using the prominent Na^+ and K^+ peaks visible even at moderate pulse energies, the position of the Ba^+ peaks is inferred to be at 37 ± 0.5 μs in the RIS spectrum, having accounted for the 1 μs RIS pulse delay and the fact that ionization due to RIS creates ions at slightly lower potentials, leading to a further delay of ~ 0.3 μs. This position of the Ba^+ RIS peak is roughly consistent with the SIMION predicted TOF of about 38.5 μs.

The predicted resolution in the SIMION simulations is shown in Figure 3.10. Each

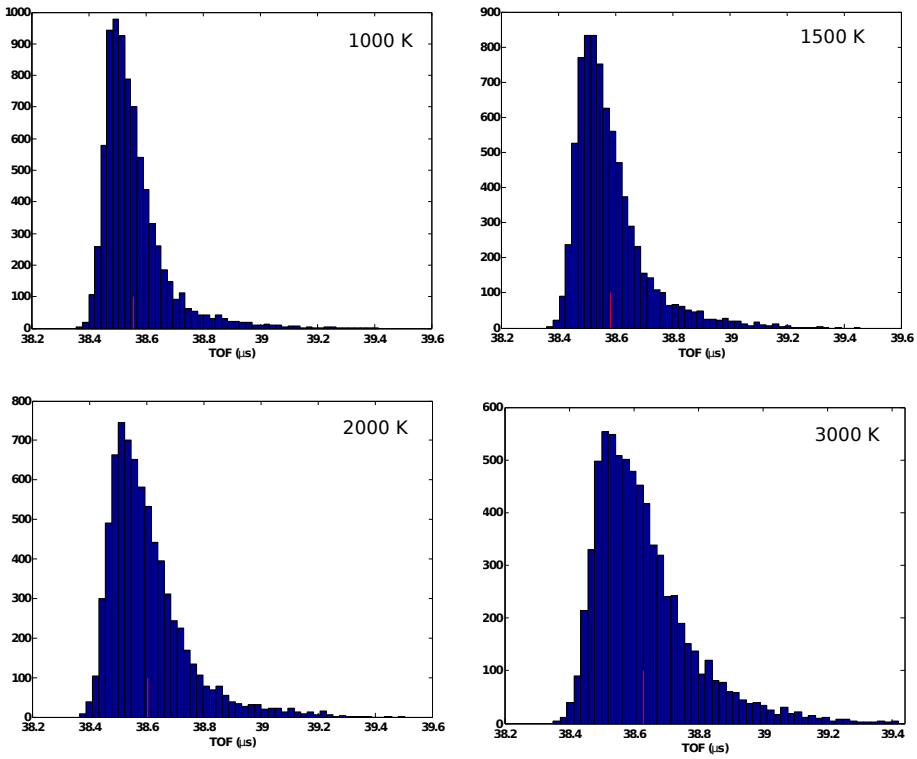

Figure 3.10: SIMION simulations of ^{138}Ba at several temperatures. These simulations show the impact of desorbed plume temperature on the resolution and time of flight of ^{138}Ba, the most common natural isotope. Higher substrate temperatures lead to lower resolutions, however even at the relatively high temperature of 3000 K the predicted resolution (using the FWHM of the peak) is $m/\Delta m = 84$. Data courtesy of S. Kravitz.

Temperature (K)	Resolution
1000	129
1500	114
2000	97
3000	84

Table 3.3: Resolutions for the ^{138}Ba peak predicted by SIMION. The resolution was assigned using the mean peak time and the FWHM of the peak.

simulation modeled a desorbed plume of neutral atoms with a thermal distribution at the given temperature, originating isotropically from the entire 5 mm $\times$ 5 mm square substrate surface. The neutral atoms in this distribution were ionized 1 μs after desorption to model the delay between the desorption and ionization lasers. This modeled the expected increase in width due to ionization away from the surface. The full width half max (FWHM) of the peaks can be used to estimate the resolution for each case, shown in Table 3.3.

Every surface tested in this work was found to have Na^+ and K^+, which were detected through direct ionization using the IR desorption laser (These species are expected to thermally desorb as ions [45]). Cleaning techniques (described in Chapter 5) were unable to completely eliminate these contaminations. In addition, directly ionized Li^+, Rb^+ and Cs^+ were observed from a Si substrate, as shown in Figure 3.11.

The resolution of the TOF was estimated in the vicinity of the expected Ba^+ signal using the $^{133}Cs^+$ peak. In this case, the mass resolution is defined as $m/\Delta m = t/2\Delta t$ [62]. Because ^{133}Cs is the only stable isotope of Cs, it generates a relatively clean signal that allows a simple Gaussian fit of the peak, shown in Figure 3.12. The full width of this peak showed a resolution of $m/\Delta m \approx 73$. This resolution is not sufficient to separate individual isotopes of Ba as in most data taken, but it is enough to separate Ba peaks from most backgrounds, including ^{133}Cs.

The resolution determined from the ^{133}Cs peak does not account for the differences in the desorption and ionization processes of all types of ions. It is expected that the directly ionized atoms leave the substrate as ions, with a thermal distribution that reflects the surface temperature of the substrate. In contrast, neutral Ba desorbed

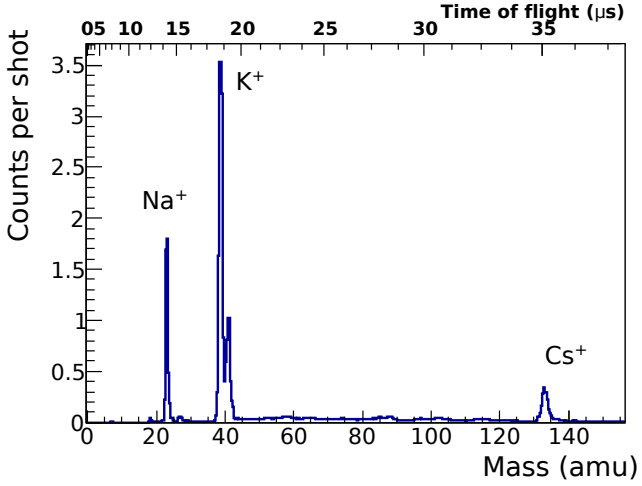

Figure 3.11: TOF spectrum showing alkali atoms directly ionized in LITD from a Si substrate. These alkali atoms are a surface contaminant. Because K^+ ions appear in most of the TOF spectrums, they can be used to calibrate the TOF. The ^{133}Cs peak is used to estimate the mass resolution of directly ionized species near the Ba region of interest, however it is not a contaminant on most surfaces. A Gaussian fit of this ^{133}Cs peak is shown in Figure 3.12.

from the substrate will be ionized at some distance from the surface depending on the thermal energies of the desorbed Ba, and on the delay between the desorption laser and the RIS lasers. Desorbed neutral Ba with higher velocities will travel further from the substrate and thus be ionized at a lower potential, which will then increase their TOF. This spatial distribution of ions may lead to slightly worse resolution of the RIS peak than of the directly ionized peaks.

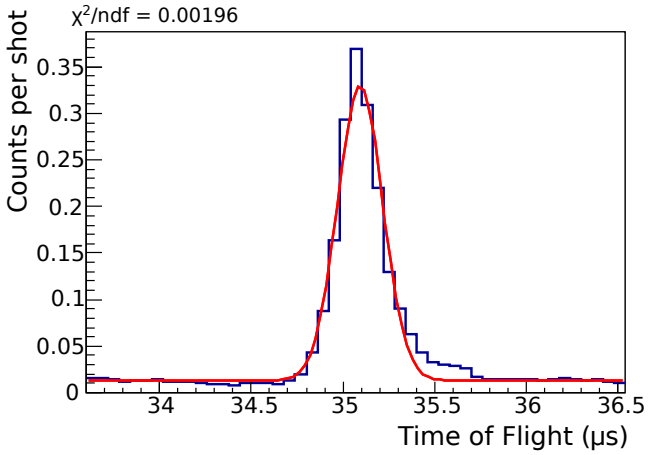

Figure 3.12: Gaussian fit of a ^{133}Cs peak. This ^{133}Cs peak comes from the dataset shown in Figure 3.11.

Chapter 4

Initial Tests of Ba Recovery

As described in Chapter 2, the selection of substrates is crucial to the efficient and selective recovery of Ba from the LXe detector. This chapter shows results of tests performed on several substrates using the device described in Chapter 3. Tests consisted of mounting substrates in the vacuum system then attempting to recover Ba through the LITD+RIS process. Substrates that appeared sufficiently clean were exposed to the Gd-driven Ba^+ source in vacuum. Tests of recovery of Ba from LXe have not yet been attempted.

This chapter describes Ba^+ signals received from tests of LITD+RIS apparatus. As noted in prior chapters, detected Ba^+ has been ionized through two processes: Ba^+ desorbed and ionized by the LITD laser ("directly ionized Ba^+"), and Ba^+ desorbed as a neutral atom by LITD and then ionized by the RIS lasers ("RIS Ba^+"). The latter process confirmed detection of Ba through the selective and sensitive process as intended in the design of this apparatus. In all cases these signals were identified by their mass as measured by the TOF spectrometer, and when appropriate, we confirmed their spectroscopic response to the RIS lasers. Results from Si, SiC, Ta, Ni, and W substrates are considered here.

Aside from signals from directly ionized Ba^+ and RIS Ba^+, the various substrates have also shown other signals potentially from molecules containing Ba. These included a peak at 157 amu/e interpreted to be BaF^+ (a known product of the Gd-driven Ba source) directly ionized by the LITD laser, and a peak desorbed as a neutral then

ionized by 535 nm laser light at mass 168 amu/e, interpreted to be $BaSi^+$. In addition, the LITD laser desorbs an array of other species that the TOF spectrometer determines to be non-Ba. While very careful setting of the LITD pulse energy can minimize non-Ba species, and subsequent optical or mass spectroscopy can easily identify Ba^+ ions, the investigation of non-Ba species is important because surface cleanliness and chemistry affect the desorption energy of Ba, the charge state of desorbed Ba and possible molecules formed by Ba.

The initial discussion is limited to Ba^+ resulting from contamination on the surfaces. In the data sets presented here the Ba "background" exceeds the quantities we expect to recover from depositions, so that we do not yet have a clean signature for Ba deliberately deposited with a $\sim$ 100 Bq source. Once we had succeeded in substantially reducing backgrounds, we tested loading of Ba from the Gd-driven source, the results of these attempts are detailed in Section 4.3. Tests in LXe using the ^{252}Cf source will be performed later. Efforts to remove surface contamination of Ba as well as non-Ba species that could affect desorption are detailed in Chapter 5. In the following section we will concentrate on the phenomenology produced by "background" Ba present on substrates without exposing them to the Ba sources.

4.1 Detection and Identification of Ba

Ba has been identified using RIS from Ta, W, Ni, Si and SiC substrates. First, the expected behavior of the signal is shown, then results from each of these substrates are discussed. Each substrate tested presented a different surface chemistry which may have affected Ba desorption.

Each substrate was cleaned before use in ultrasonic baths of acetone then ethanol for 15 minutes each. This ultrasonic cleaning with solvents was expected to remove dust and oils from the substrate; however, Ba adsorbed directly to the substrate may not have been removed. In addition, the Si substrate was cleaned by an etching technique used to prepare Si for fabrication, described further in Section 4.1.4.

Figure 4.1 shows a typical TOF spectrum from a Ta foil substrate, including directly ionized Ba^+, RIS Ba^+, and directly ionized BaF^+. Both the cases of RIS

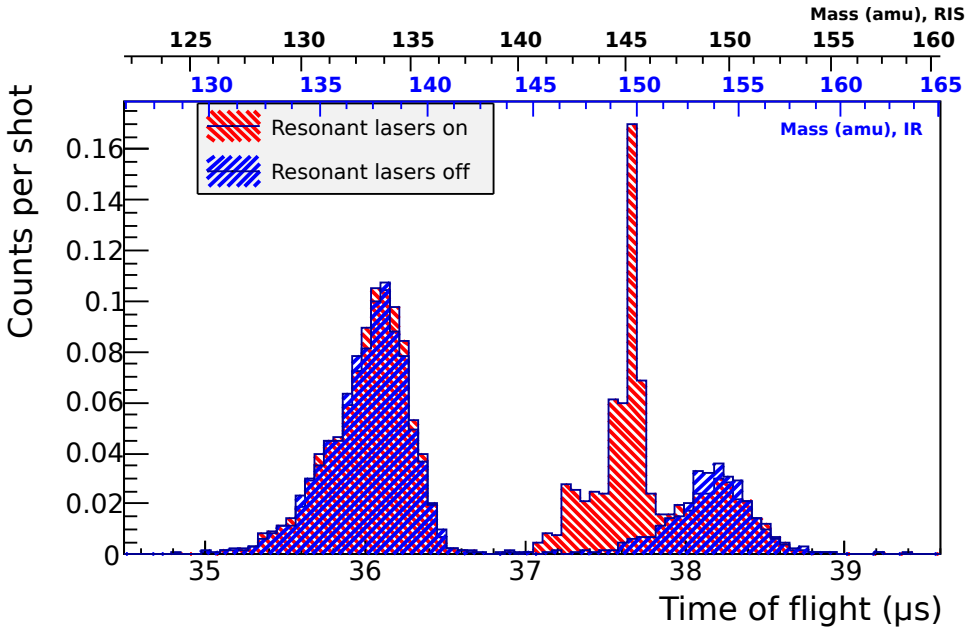

Figure 4.1: TOF spectrum from a Ta substrate, showing directly ionized Ba^+, RIS Ba^+ and directly ionized BaF^+. The RIS Ba^+ peak is delayed slightly more than the 1 μs laser delay due to the ionization occurring at a lower potential than the directly ionized Ba^+. This is the dataset used in the laser blocking test shown in Figure 4.2, thus the RIS Ba^+ peak is somewhat reduced due to blocking the RIS lasers. Two mass scales are printed above the time of flight: the IR mass scale is for ions produced during the LITD laser pulse, while the RIS mass scale is for ions produced during the RIS laser pulse. Because ions produced during the RIS laser pulse are created off the substrate at a lower potential, the laser delay alone may not account for the entire shift in the TOF, leading the mass scale to be slightly off.

lasers on (red histogram) and off (blue histogram) are shown. The peak appearing in the red histogram but not the blue histogram corresponds to RIS Ba^+, a confirmation of the expected selective detection of Ba^+.

The appropriate spectroscopic response to the RIS lasers was confirmed in this dataset by blocking each laser in turn, as shown in Figure 4.2. The upper half of the plot shows the number of counts in the RIS Ba^+ window, between 37 and 37.9 μs in Figure 4.1. The lower plot shows the photodiode measurements, indicating which RIS laser is blocked. When either RIS laser was blocked, the RIS Ba^+ signal decreased. The count rate did not drop to zero because the tail of the BaF^+ peak overlapped

the RIS Ba^+ window, as shown in Figure 4.1.

Because contamination was observed on material from the same stock, this Ba was assumed to be contamination as well; however, for completeness we must note that this substrate had been exposed to the Gd-driven source. Tests on this substrate prior to the deposit did not use adequate LITD pulse energies to show Ba. We believe that this exposure did not affect the amount of Ba detected.

4.1.1 Tantalum Substrates

Ta substrates are of interest because they can withstand high temperatures during LITD (the melting temperature of Ta is 3269 K), which can offset a higher desorption energy. Ta samples tested in this system included rolled foils and polished polycrystalline substrates.

Tests of Ta substrates showed Ba^+, RIS Ba^+ and BaF^+ from contaminations, as shown in Figure 4.1. As described above, these contaminations were useful for determining the appropriate spectroscopic response. Using laser cleaning and electron gun heating, we were not able to reduce the Ba backgrounds enough to measure deposits of Ba from the Gd-driven source.

4.1.2 Tungsten Substrates

W substrates showed similar signals to Ta substrates. W is promising because it has a high melting point (3683 K) and literature reports desorption energies of $E_{\text{des}} = 3.38$ eV [35]. This combination of high melting point and moderate desorption energies may allow desorption probabilities of a few percent in a single LITD laser shot. TOF spectra from polished polycrystalline W substrates showed directly ionized Ba^+, RIS Ba^+, and directly ionized BaF^+ without exposure to the Ba source. As with Ta, the source of this contamination is not known, but could have come from the bulk material or the local environment. Laser cleaning (Described in Section 5.1) was unable to completely remove evidence of Ba from the TOF spectrum. Because it appeared that Ba remained on the surface, we did not test loading in this case.

A W layer deposited on a Si wafer was also tested. This substrate allowed resistive

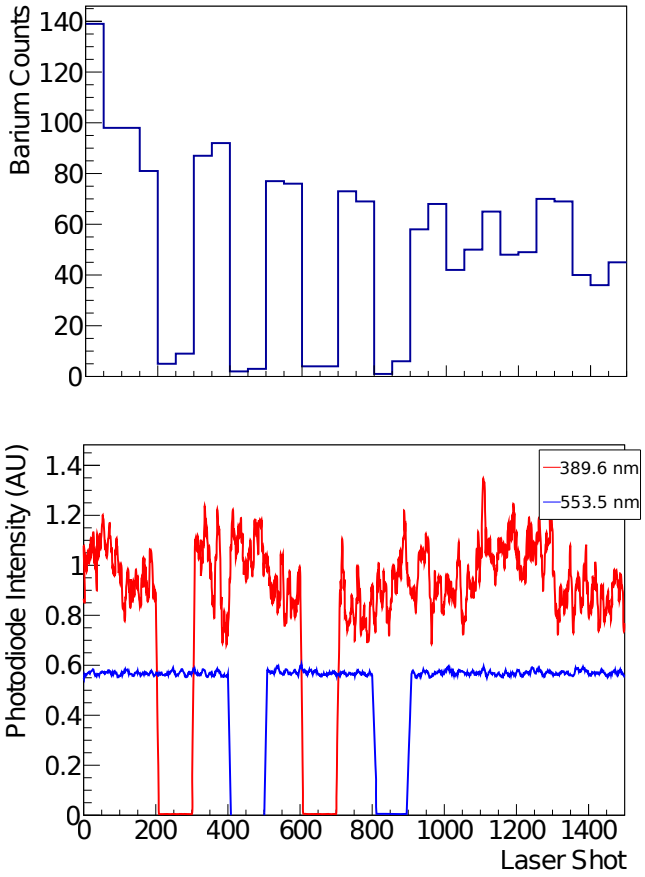

Figure 4.2: RIS dependence of the Ba peak can be demonstrated by blocking either of the RIS lasers. The top panel shows the counts from the RIS signal window from 37 to 37.9 μs in Fig. 4.1. Blocking either laser—shown when the photodiode associated with that laser drops—reduces the number of counts in the RIS window.

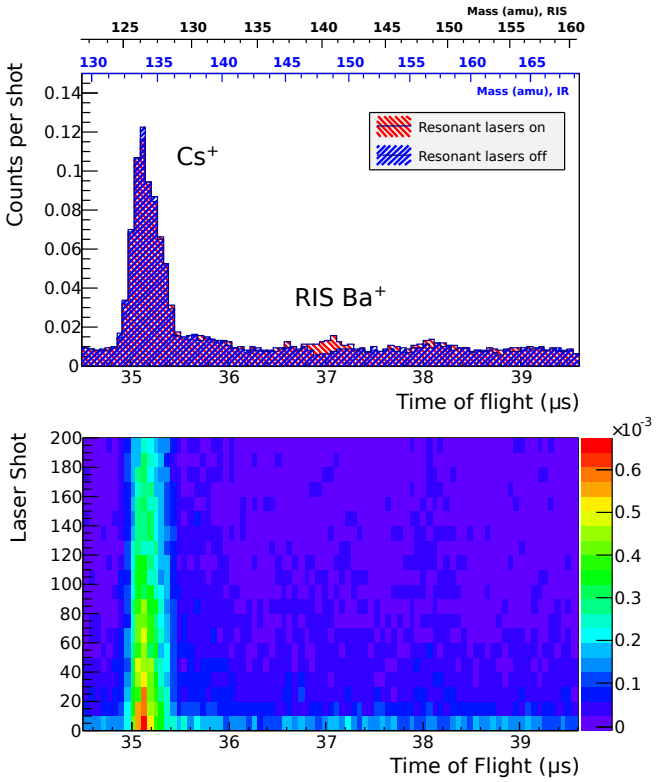

Figure 4.3: RIS Ba from a W substrate deposited on a Si wafer. This substrate was not exposed to the Gd-driven Ba^+ source. This substrate was heated to 800°C for one hour, then to 1200°C for 30 seconds.

heating, which produced a small Ba^+ peak even before exposure to the Gd-driven source, shown in Figure 4.3. Heating was initially intended to clean the substrate, but in most cases it increased the Ba^+ background. This technique is discussed further in Section 5.2. Laser cleaning eliminated the Ba^+ background peak from the TOF, then the substrate was exposed to the Gd-driven source overnight. The TOF spectrum showed a directly ionized BaF^+ peak after loading, but not an RIS Ba^+ peak or a directly ionized Ba^+ peak. The observation of BaF^+ after exposure to the Gd-driven source is described in more detail in Section 4.3.

4.1.3 Nickel Substrates

Ni substrates were tested since some literature has suggested that the desorption energy is 2.9 eV [36]. A laser pulse that heats the Ni substrate up to 1720 K (near Ni's melting point of 1728 K) gives a probability of desorption of 2×10^{-5}. A polished Ni substrate was mounted in the same fixture that had held the Ta and W substrates. Tests of the Ni substrate showed smaller amounts of Ba due to contamination compared to W, Ta and Si substrates. A TOF spectrum from a polycrystalline Ni substrate is shown in Figure 4.4. Laser scans were able to remove this background Ba^+. Once cleaned, this substrate was exposed to the Gd-driven source for 1 hour, but this deposit did not increase signals from directly ionized Ba^+, RIS Ba^+ or directly ionized BaF^+. Overnight loading was not attempted with this substrate; however, the cleanliness of the substrate and the possibility of acquiring ultra pure Ni substrates may allow further research.

4.1.4 Silicon Substrates

Silicon wafers have very high purity and have been used in Ba adsorption studies at very small coverages [63]. In addition to this extremely high purity, monocrystalline Si wafers can provide uniform surfaces with specific crystal orientation. This orientation determines some of the chemical properties of the substrate: Si (100) has 2 dangling bonds per surface atom, while Si (111) has 1 dangling bond per surface

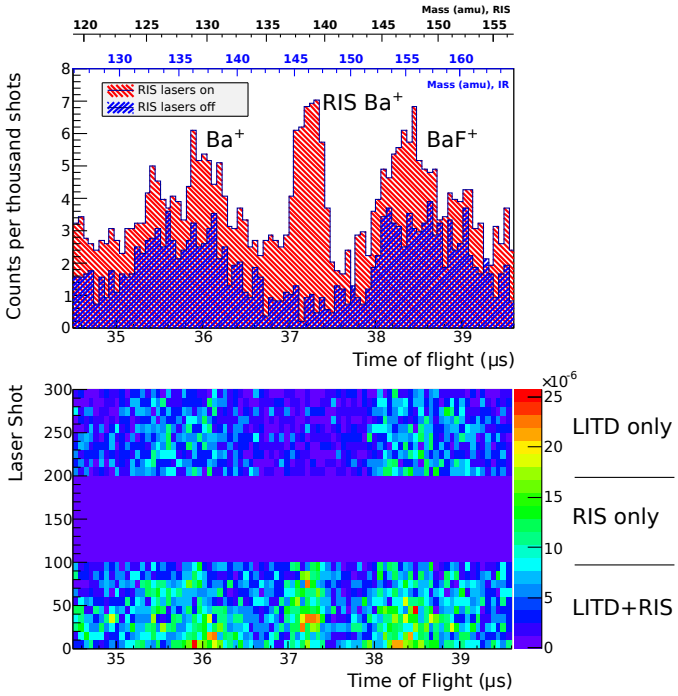

Figure 4.4: RIS Ba signal from Ni. The upper panel shows the TOF in the region of the Ba^+ peaks. The red histogram shows ions collected when all lasers (LITD+RIS) were on, while the blue histogram shows ions collected when only the LITD laser was on. The lower plot illustrates the data taking cycle: shots 0-100 are LITD+RIS, shots 100-200 are RIS only, and shots 200-300 are LITD only. All times of flight have more counts in the first cycle because the LITD laser cleans the surface over the course of the first 100 shots. Note that the RIS Ba^+ peak does not reappear in shots 200-300, confirming the RIS dependence of this peak.

atom [27]. While the purity and surface properties of Si wafers are convenient, insulating substrates may charge up during LITD, affecting the electric fields near the substrate and altering the TOF of Ba^+. For this reason, all semiconductor substrates used in this system were heavily doped to be conductive.

We have performed several tests with heavily doped Si substrates. Both Si (100) and Si (111) have been tested, however the most detailed tests shown here were performed on Si (100). A heavily doped Si (100) substrate was cleaned before insertion using the recommended chemical etching procedure at the Stanford Nanofabrication Facility (SNF). This consists of four steps: An initial dip in a sulfuric acid/H_2O_2 solution; 10 minutes at 50°C in 5:1:1 H_2O:H_2O_2:NH_4OH; 30 seconds at room temperature in 50:1 H_2O:HF; and finally 10 minutes at 50°C in 5:1:1 H_2O:H_2O_2:HCl (all ratios by volume). This etching procedure was expected to remove surface contaminants and oxide layers on Si wafers.

The TOF spectrum from this Si (100) showed small peaks from RIS Ba^+ as well as directly ionized Na^+, K^+, Ba^+ and BaF^+ from surface contamination that remained despite the chemical treatment. The TOF in the region of Ba^+ is shown in Figure 4.5. In an attempt to eliminate the Ba contamination, the substrate was heated to 700°C for 1 hour, then to 1050°C for 30 seconds. Heating the substrate greatly increased the Ba signals in the dataset taken immediately afterwards, as shown in Figure 4.6. This effect was observed on Si (111) and some metal substrates. The results from a Si (111) substrate are shown in Figure 4.7. Other Si (100) substrates had similar contaminations to this substrate despite a variety of preparations.

The desorption energy of Ba on Si (100) has been experimentally determined to be 3.5 eV [64]. This desorption energy can be used to calculate probability of desorption for a single atom in a single laser shot to be $P_{\mathrm{des}} = 5 \times 10^{-9}$ using Equation 2.2 and the heating profile shown in Figure 2.2. Despite this very small probability of desorption, we have detected both directly ionized Ba^+ and RIS Ba^+ from several Si substrates. It is possible that the Ba is not bound to the substrate as in reference [64] or that the level of contamination is much higher than expected.

Several studies reported that substrate heating was insufficient to remove all Ba from the Si substrates [64, 65]. These studies suggested that the strong Ba-Si bond

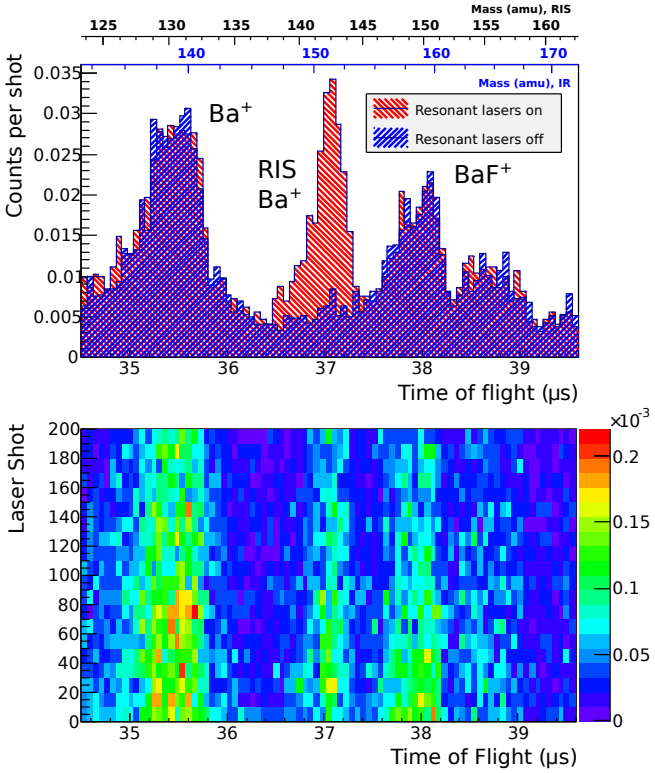

Figure 4.5: RIS Ba^+ signal from Si (100) prior to heating. The upper panel shows the TOF in the region of the Ba^+ peaks. The red histogram shows ions collected when all lasers (LITD+RIS) were on, while the blue histogram shows ions collected when only the LITD laser was on. The lower panel shows the decay of these peaks over the data taking cycle summed over all locations. The lasers were cycled between LITD+RIS and LITD only every other shot. This substrate was etched at the SNF before insertion.

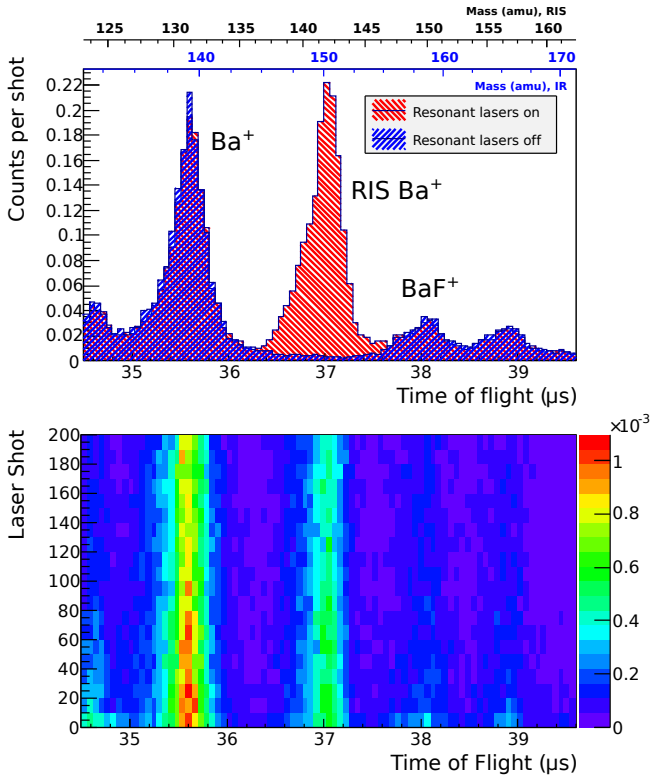

Figure 4.6: RIS Ba signal from Si (100) after heating. The upper panel shows the TOF in the region of the Ba^+ peaks. This substrate was cleaned chemically before insertion then heated to 700°C for 1 hour, then to 1050°C for 30 seconds before this dataset was taken.

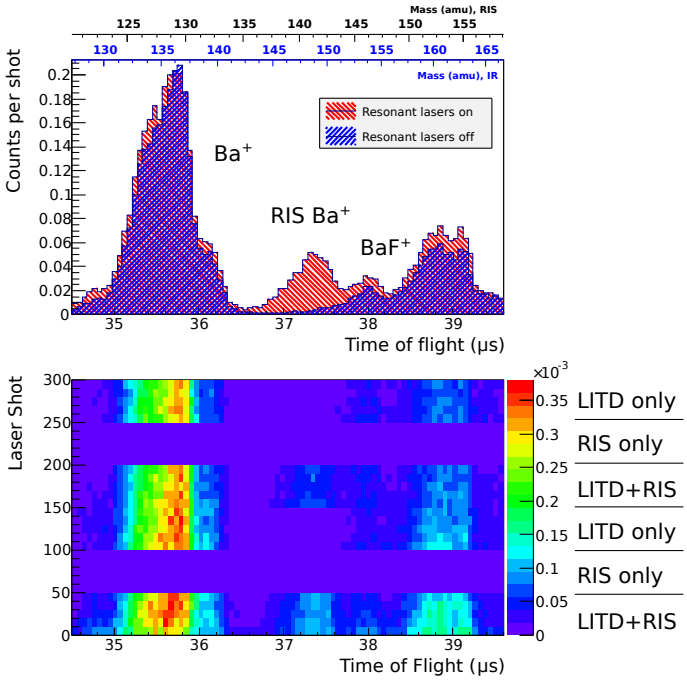

Figure 4.7: RIS Ba signal from Si (111) after heating. The upper panel shows the TOF in the region of the Ba^+ peaks. This substrate was cleaned ultrasonically before insertion then heated to 1000°C for 1 hour. This substrate had not been exposed to the Gd-driven Ba^+ source.

prevented thermal desorption of Ba, requiring Ar^+ sputtering to recover a Ba-free substrate. Some studies described Ba-induced surface reconstructions, which supported evidence that the Ba-Si bond is very strong and indicate that upon heating adsorbed Ba became part of the surface structure rather than desorbing [64, 66, 67]. The LITD process may have provided the required heating to make this reconstruction.

This system does not have the ability to measure Ba-induced surface reconstructions, but evidence of $BaSi_n$ molecules has appeared in some tests of desorption and ionization from Si (100). In an attempt to use 535 nm light to ionize BaO, as described in [68], we detected a 168 amu/e signal desorbed as a neutral then ionized by 535 nm light, shown in Figure 4.8. Because this calibration slightly overestimates the masses of species ionized by the delayed lasers, this peak was interpreted to be $BaSi^+$. BaO^+ (153 amu/e) was not detected in the TOF spectrum, despite the likely presence of adsorbed O on the surface from residual O_2, H_2O, CO_2 and CO.

It is possible that heating the substrate promoted silicide formation, which would have reduced the efficiency of recovery of deposited Ba. Low Energy Electron Diffraction (LEED) and Ultraviolet Photoelectron Spectroscopy (UPS) studies showed that BaSi forms at $300 - 600°C$, and heating to 700°C forms $BaSi_2$ [69, 70]. Evidence of silicide formation at room temperature was found in synchrotron-radiation photoemission studies of Ba on Si (100) [71].

Moreover, if indeed barium silicide forms at high temperatures at submonolayer Ba coverages, it is possible that it forms due to heating during the LITD pulse. The TOF spectrum shown in Figure 4.8 indicates that barium silicide formation is likely. Silicide formation on the surface leads to decreased efficiency of detection, since Ba desorbs as a BaSi molecule, which cannot be ionized by our standard RIS scheme. It is not known how much this decreased the efficiency since the fraction of Ba on the surface bound in $BaSi_n$ was not known.

In addition to losses in efficiency due to formation of barium silicide, diffusion of the adatom into the substrate could cause a loss of efficiency in the Ba recovery process. Studies have shown that Ba diffuses into Si at a temperature of 800°C with as little as 0.006 monolayer coverage [72]. Our system does not have the capability to measure the diffusion of Ba into the substrate, so we cannot rule out that Ba diffuses

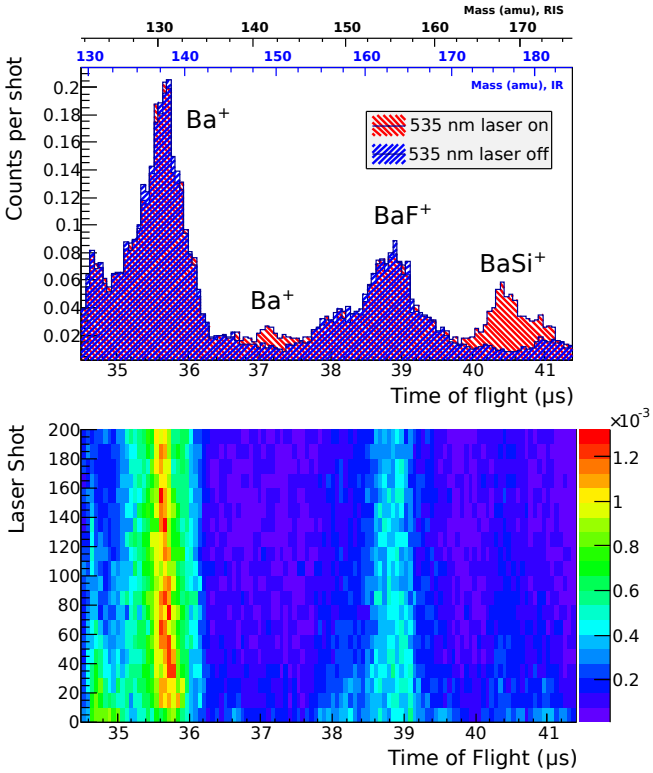

Figure 4.8: $BaSi^+$ from a Si (100) substrate. The peak at 168 amu/e was interpreted to be $BaSi^+$ ionized using 535 nm laser light. The technique is the same as used for RIS Ba, with the ionization laser following 1 μs after the desorption laser. Detuning the 535 nm light from the resonance shown in [68] did not show the line shape expected for BaO.

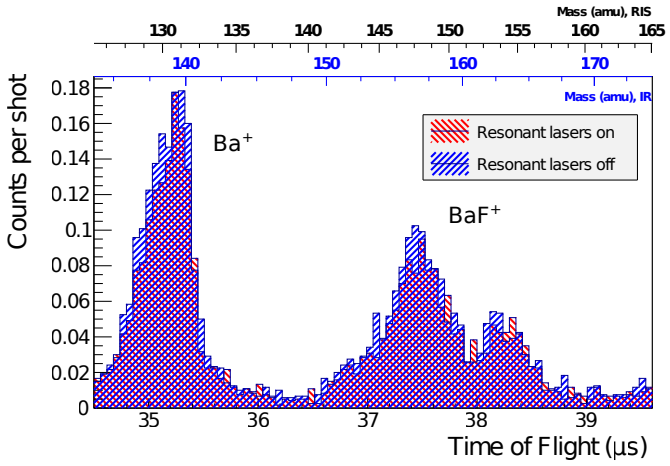

Figure 4.9: Directly ionized Ba^+ and BaF^+ from 6H-SiC (0001) before heating or exposure to the source. Note the absence of RIS Ba^+, which appeared after the substrate was resistively heated, as shown in Figure 4.10.

into the substrate during LITD.

Despite detection of strong Ba signals on Si substrates, it is clear that silicide formation, the inability of thermal desorption to remove all Ba, and diffusion into the substrate could limit the efficiency of detection of Ba atoms from Si. Because of the contamination and silicide formation issues, Si substrates are not good choices for Ba transport.

4.1.5 Silicon Carbide Substrates

LITD+RIS has been used to identify Ba from SiC grains extracted from meteorites [73, 74]. Commercial SiC wafers are available in many different polytypes (crystal structures) and crystal orientations. The wafer chosen must be conductive both to prevent chargeup during LITD and to allow resistive heating as a surface cleaning technique. A nitrogen-doped 6H-SiC (0001) wafer was chosen for this purpose. However, a bulk material assay from the vendor showed 14 ppm Ba in the bulk of the material, a contamination level easily detectable with this system and enough to overwhelm any deposit from the Gd-driven source.

Initial tests of the SiC substrate showed directly ionized Ba^+ and BaF^+ but not

RIS Ba^+, shown in Figure 4.9. After heating the substrate, the RIS Ba^+ peak appeared as shown in Figure 4.10.

Directly ionized BaF^+ is present in the TOF spectrum, as well as a peak at 162 amu/e, which was interpreted to be BaC_2^+ due to the presence of C in the substrate. All directly ionized peaks in Figure 4.10 showed a rapid decrease over the data-taking cycle, which in this case gave the appearance of a slight RIS excess because the peak decreases in the first 50 laser shots. Later datasets (including the Si (100) data shown above) cycled the lasers every other shot to reduce the effect of this decrease.

Surface preparation may help explain the presence of directly ionized peaks and the rapid decay of those peaks. 6H-SiC (0001) grows a heteroepitaxial layer of graphene when heated [75, 76]. This graphene layer can be a single sheet thick, or several sheets thick, depending on the conditions of growth. *Ab initio* models of Ba adsorption on graphene show that the desorption threshold is 0.7 eV with 0.86 e charge transfer from the adsorbed Ba to the graphene [77, 43]. The low threshold suggests that Ba desorbs easily as an ion from a graphene substrate, resulting in a relatively large directly ionized Ba^+ peak.

While the LITD+RIS system cannot identify graphitized SiC *in situ*, graphitization of a SiC substrate was identified on one of the substrates used here using X-ray Photoelectron Spectroscopy (XPS). XPS shows graphitization through a splitting of the carbon C1s peak [78], as shown on one 6H-SiC (0001) substrate used for LITD+RIS in Figure 4.11. This suggests that the large directly ionized Ba^+ peak detected in LITD tests was related to the low desorption energy from the graphitized surface. Despite the contamination in this particular sample, graphitized SiC and other graphene substrates are possibly good substrates for Ba transport.

4.2 Laser Induced Thermal Desorption Results

As described in Section 2.2, the appropriate regime for LITD must heat the surface enough to desorb Ba adatoms, but not enough to melt or ablate the substrate. Understanding the LITD process is crucial because it can generate backgrounds to the

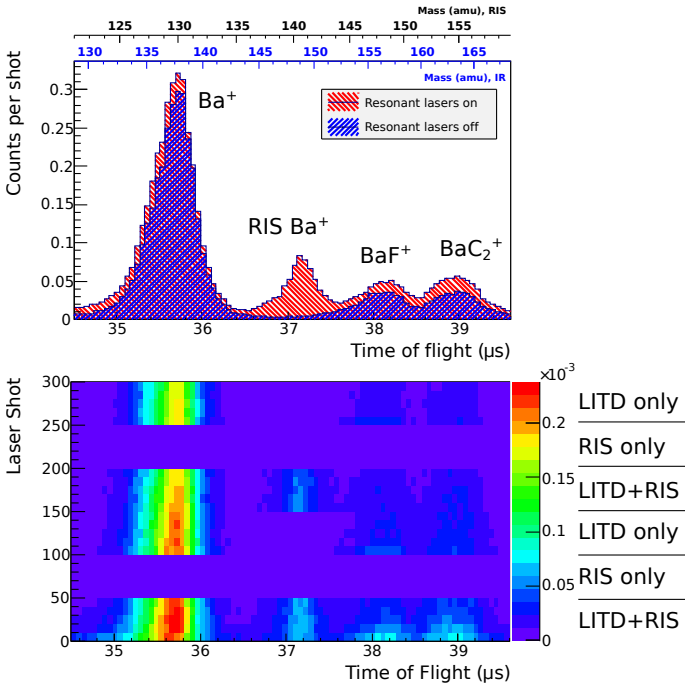

Figure 4.10: Directly ionized Ba^+ and RIS Ba^+ from 6H-SiC (0001). This sample was heated, which could have graphitized the surface. If indeed heating has graphitized the substrate, it could explain the large peak of directly ionized Ba^+. This particular dataset suffered from a very low UV power leading to a reduced RIS peak. The lower panel shows the response of the peaks over time, starting with the first laser shot at each location at the bottom, progressing upward. Shots 0-50 have both the LITD+RIS lasers, 50-100 have only the RIS lasers, 100-150 have only the LITD laser, then the same cycle repeats for shots 150-300. The BaF^+ and BaC_2^+ peaks appear to be RIS-dependent, but they are not. They decay quickly within the first 50 shots, which happen to be LITD+RIS.

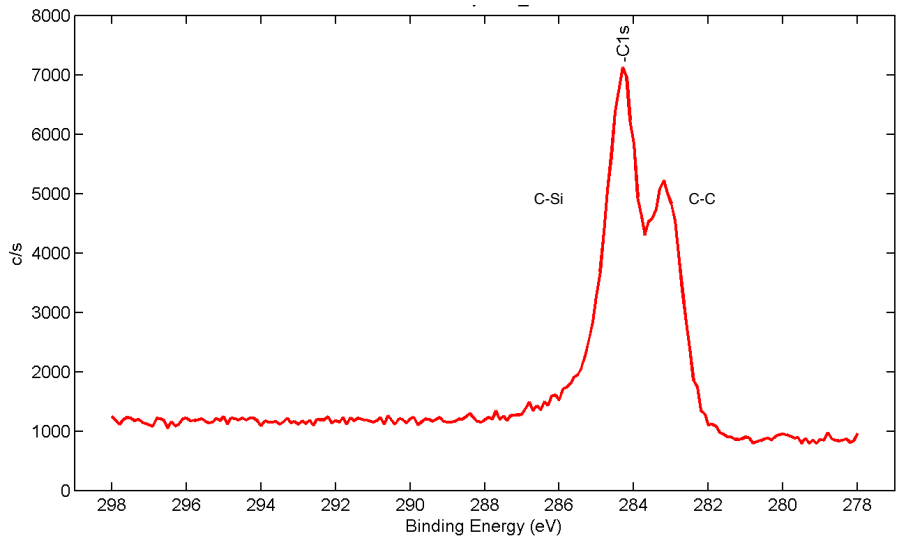

Figure 4.11: XPS scan of the C1s peak showing splitting indicative of graphitization of an 6H-SiC (0001) substrate.

RIS Ba^+ signal. While LITD should not ionize desorbed atoms, it was found that LITD pulse energies large enough to desorb directly ionized Ba^+ and neutral Ba were above the threshold for desorption of directly ionized K^+.

We tested the desorption thresholds of ions and atoms to understand better the signals produced during LITD. The desorption thresholds of different ions from Si (100) were determined by increasing the desorption laser intensity at a single location on the substrate known to produce Ba^+ as well as K^+. The count rates of a few peaks measured while increasing the desorption laser power are shown in Figure 4.12. At very low intensities, no ions were produced. The first ion to desorb was K^+, later followed by Ba^+ and RIS Ba^+. Additionally, Ba^+ was desorbed as an ion at roughly the same threshold as it was desorbed as a neutral atom (here detected using RIS). It should be noted that the number of adatoms is expected to decrease with continued LITD, as the number of adatoms decreased. This depletion may have reduced the number of counts at higher laser powers because they were taken later.

A very similar behavior was seen on a Ta substrate (Fig. 4.13): as the desorption laser pulse energy was increased, the K^+ peak appeared first, followed by the Ba^+ peaks. The appearance of K^+ ions before Ba^+ ions was expected, since the ionization

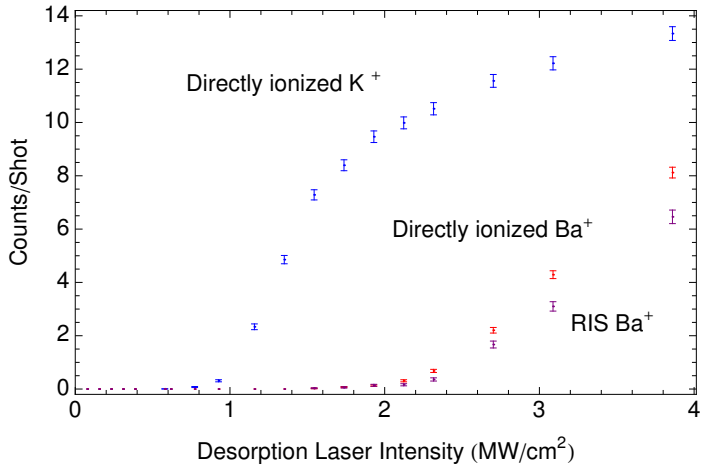

Figure 4.12: Desorption thresholds from Si (100) for directly ionized atoms and molecules as well as neutral Ba subsequently ionized through RIS. As the desorption laser intensity is increased, more ions are desorbed. This illustrates that each ion has a different threshold for desorption. Error bars shown are statistical.

energy of alkali atoms is relatively low. More surprisingly, neutral Ba desorbed at the same laser intensity as Ba^+ ions. This similarity between Si and Ta may be an indication that the adsorbates that we observed in the TOF spectrum were not bound to the substrate, rather to other adsorbates, such as O.

The Saha-Langmuir equation [79] predicts increasing ionization rate with increasing temperature in surface ionization processes, but we did not observe this effect. Instead, as the desorption laser intensity (and thus also the surface temperature) was increased, the ratio of directly ionized Ba^+ to RIS Ba^+ did not increase significantly, as shown in Figure 4.14.

It is possible that the constant ionization rate versus temperature was due to adsorbed molecules that dissociate into ionic species. BaO deposited on Ta has been shown to emit Ba^+ when heated [31, 32]. If there was BaO adsorbed on the substrate, the thermal dissociation of this molecule (or other similar molecules, such as BaF^+ deposited from the Gd-driven ion source [54]) could have accounted for more directly ionized Ba^+ than expected. BaO was not detected on Si substrates in the tests described in Section 4.1.4; however, it may be present on other substrates. The efforts to clean the substrate of potential reactants that could create such molecules

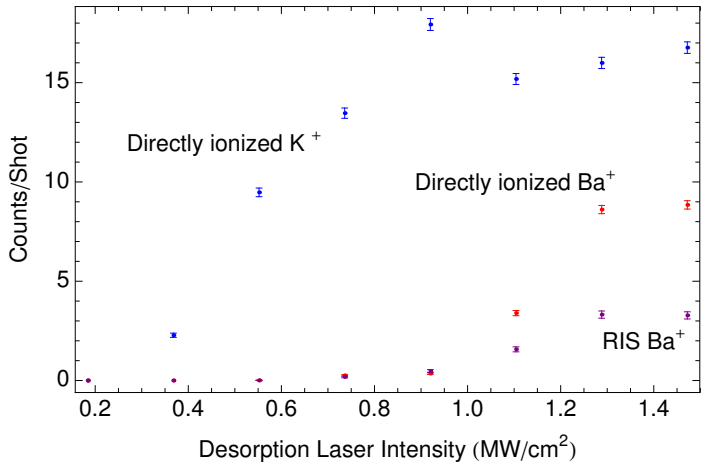

Figure 4.13: Desorption thresholds on Ta. Note the similarity between this and the same test on Si, shown in Figure 4.12. This is an indication that Ba is bound in the same way on both these substrates. Errors shown are statistical.

are described in Chapter 5.

The electron transfer from the adatom to the substrate may affect the ratio of Ba ions to neutral Ba desorbed. Low-energy deuterium scattering has shown that K adatoms bond ionically to Si (100) substrates [80], but Ba adatoms bond covalently to Si (100) substrates [81]. DFT calculations suggest that only 0.15 e of charge is transferred from the adsorbed Ba atom to the Si (100) substrate [41], indicating a partially ionic bond. If the electron transfer to the substrate determines the fraction of desorbed ions, less electron transfer to the substrate would allow more Ba to desorb as a neutral atom for selective ionization using RIS.

4.3 Tests of Deposit in Vacuum

Substrates that had been cleaned to reduce the Ba background were exposed to the Gd-driven Ba source, which is known to produce Ba^+ and BaF^+, as well as neutral Ba atoms [54]. Although the Si substrates had been clean enough to test deposition of Ba, overnight exposure to the source with the substrate biased to -230 V did not reveal an increase in directly ionized Ba^+ or RIS Ba^+, only directly ionized BaF^+ (Figure 4.15). In this case, a Si substrate was measured to have no BaF^+ (blue histogram) after

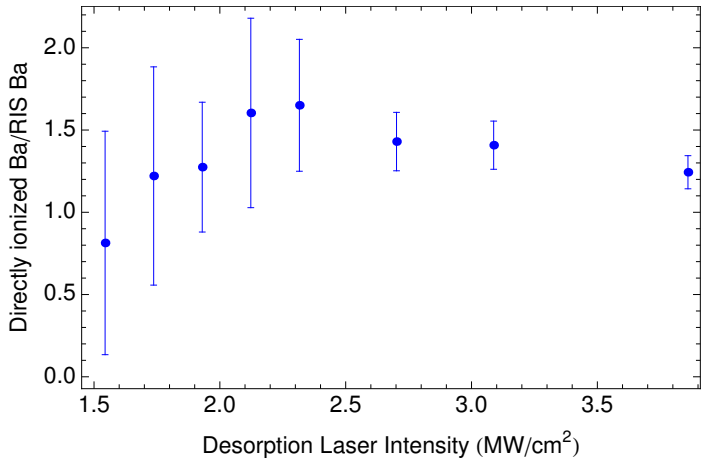

Figure 4.14: Ratio of directly ionized Ba^+ to RIS Ba^+ at several LITD intensities. Each datapoint is the average of power increase data for three separate locations on a single Si (100) substrate. Error bars are statistical.

laser cleaning (as described in Section 5.1). The substrate was then exposed to the Gd-driven Ba^+ ion source for 15 hours, then tested again (red histogram). A peak appeared at the appropriate mass for BaF^+, indicating the effective deposition of a BaF^+ molecule on the substrate. Since Gd-driven sources emit BaF^+ ions, it is possible that BaF^+ adsorbed to the substrate during exposure to the source desorbed as BaF^+ during LITD.

The BaF^+ peak decayed away very rapidly, as shown in Figure 4.16. The decay was consistent between the LITD+RIS (shots 1-50 and 101-150) and the LITD only (shots 51-100 and 151-200), indicating that this peak had no RIS-dependency. The rapid decay of this peak (vanishing within 200 laser shots) indicates that the desorption energy E_{des} of this molecule was relatively low[1]. This measurement was repeated on Si (111) cleaned of traces of BaF^+. Exposure to the Gd-driven source caused the appearance of the BaF^+ peak after 14 hours of deposition (once again the substrate was biased to -230 V), shown in Figure 4.17. This peak decayed quickly, similarly to the deposited BaF^+ peak on Si (100). The deposit also created a quickly-decaying shoulder on the Si_5^+ peak. The RIS dependence of these peaks is shown in more detail in Figure 4.18. The shoulder on the Si_5^+ peak decayed within the first laser

[1]Measurement of E_{des} would require measurement of the surface temperature over the laser pulse.

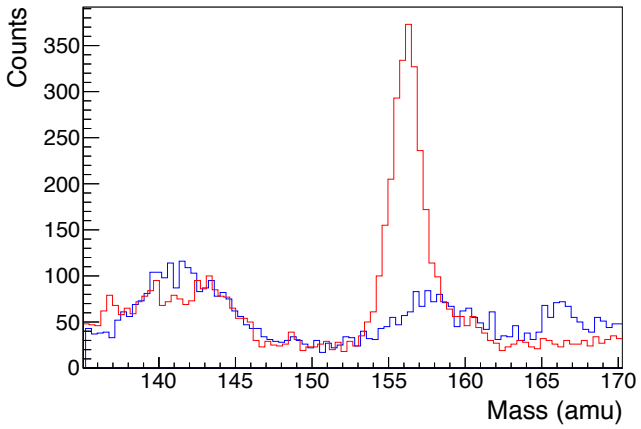

Figure 4.15: Deposition and detection of BaF^+ on a Si (100) substrate. The substrate was exposed to the Gd-driven Ba source, which is known to produce BaF [54], for 15 hours. After exposure, there is a new peak at 157 amu/e. This peak disappears within the first 200 laser shots at each location, as shown in Figure 4.16. Prior to this test, the substrate was cleaned by laser cleaning.

cycle, thus it appeared to be RIS-dependent, however faster laser cycling on the W substrate showed a peak at a similar TOF to be directly ionized.

The W substrate deposited on a Si wafer was cleaned then exposed to the Gd-driven source for 17 hours while biased to -230 V. Figure 4.19 shows the TOF spectrum in the region of interest before and after the exposure. As on the Si substrates shown above, exposure to the source caused a large increase in the BaF^+ peak, and once again there was an increase in the peak at 144 amu/e. The detailed RIS laser dependence of this peak is shown in Figure 4.20. It appears that this peak was not dependent on the RIS lasers.

The appearance of BaF^+ after exposures to the Gd-driven source allowed an estimate of the efficiency of recovery of Ba, albeit as a molecule and without the spectroscopic confirmation desired. An approximate efficiency of recovery was estimated using the emission of the Gd-driven source. The decay rate of the source is 178 Bq, with 5.2 Ba produced per ^{144}Sm recoiling through the BaF_2 layer [54, 49]. In this system the substrate was placed 1 cm in front of the source such that the solid angle subtended by the 5 mm $\times$ 5 mm substrate was about 0.02 steradian. Using these

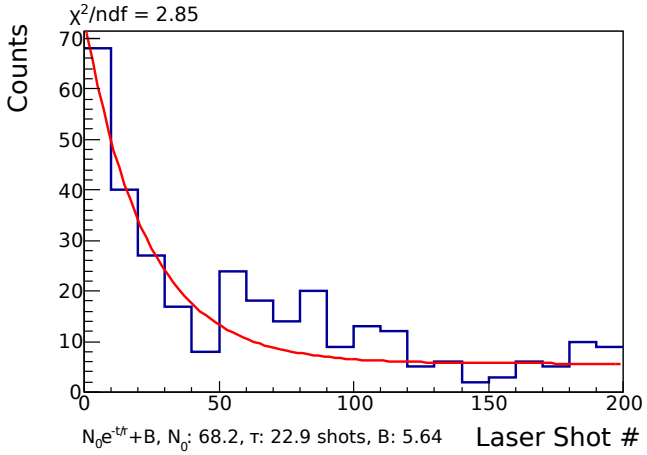

Figure 4.16: Deposited BaF^+ peak decay at a single location on Si (100). This tracks the decay of the deposited BaF^+ peak shown in Figure 4.15.

Substrate	Load Time (hrs)	Ba deposited	BaF^+ recovered	Efficiency
Si (111)	14	940000	1100	0.12%
Si (100)	15	1000000	2300	0.23%
W	17	1140000	5700	0.50%

Table 4.1: Recovery of BaF^+ from Si (111), Si (100) and W.

parameters, it was expected that the source deposited 18.6 Ba/second. This estimate of the loading rate used only this solid angle treatment, without accounting for the charge state of the Ba or the molecules formed. Table 4.1 shows the total Ba loaded, compared to the number recovered for the Si (111), Si (100) and W substrates described in this section. The recovery of BaF^+ was as high as 0.5% from the W substrate. Future improvements to this efficiency will come through understanding how BaF^+ bonds to the substrate and what fraction of BaF^+ bound to the substrate desorb as ions.

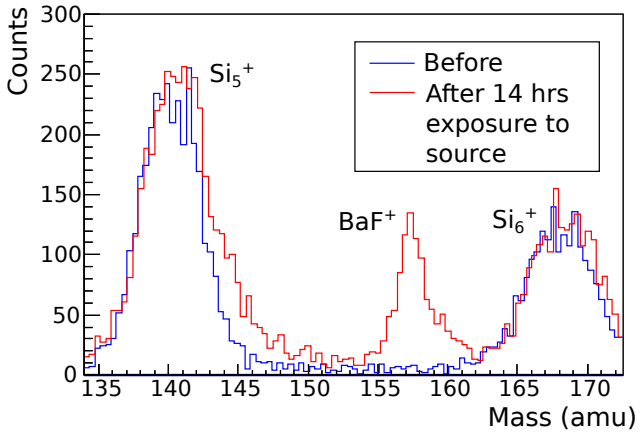

Figure 4.17: Deposited BaF^+ peak on Si (111). The blue data show the TOF in the region of interest before exposure to the source, the red data show an identical scan after 14 hours exposure to the Gd-driven source. A large peak appears at 157 amu/e, interpreted to be BaF^+. The added shoulder on the right hand side of the Si_5^+ peak was not dependent upon the RIS lasers in other datasets, thus this was not interpreted to be RIS Ba^+. The TOF spectrum from the dataset after loading is shown in more detail in Figure 4.18. This particular substrate was damaged in an attempt to clean the substrate using resistive heating, leading to large Si_n^+ cluster peaks shown. This damage is discussed in more detail in Section 5.2.

4.4 Summary of Results

LITD+RIS has allowed detection of Ba^+ on several different substrates even before exposure to the Gd-driven Ba^+ source, including Si, SiC, Ni, W, and Ta. A brief summary of results from these substrates is shown in Table 4.2. The signals come from contaminations and Ba^+, RIS Ba^+ and BaF^+. The amounts of Ba detected from these tests varied widely and did not appear to be related to the preparation of the substrate or the desorption parameters used; instead, they appeared to be due to preexisting contamination of the various substrates. The large variation in the surface temperatures at a given desorption laser pulse energy may have been due to the different light adsorption properties of these substrates. This alone may account for some of the wide variation in Ba^+ detection rates. Understanding what factors influence detection of Ba^+ remains a challenge for this project.

There is some evidence that Ba forms $BaSi_n$ when deposited on Si substrates, and it is possible that it forms molecules with other adsorbates and substrate atoms. Because molecules are not ionized by the RIS lasers, the substrate must be chosen to limit molecule formation.

Deposit from the Ba source produced only a BaF^+ signal, not a directly ionized Ba^+ or RIS Ba^+ signal that could be indicative of Ba adsorbed as an atom. Further efforts must be directed towards understanding the best substrate and surface preparations to enable neutral Ba desorption required for efficient recovery and identification of Ba using RIS. This preparation will require a full understanding of the surface chemistry.

Substrate	Preparation	LITD Intensity (MW/cm^2)	Ba^+ (per shot)	RIS Ba^+ (per shot)	BaF^+ (per shot)
Si (100)	SNF preparation, Laser cleaned, Heated.	5.8	1.5	1.7	0.29
Si (111)	Ultrasound, Laser cleaned, Heated 1000°C 1 hour.	1.6	2.5	0.61	0.15
6H-SiC (0001)	Ultrasound, Laser cleaned.	0.66	0.063	0	0.045
W	Ultrasound, Heated.	0.64	0.95	0.41	0.38
Ni	Ultrasound, Laser cleaned.	0.39	0.09	0.15	0.13
Ta	Ultrasound, Heated for 5 mins.	0.41	1.3	0.53	0.51

Table 4.2: Ba detection on several substrates prior to exposure to the Ba source. The large variation in Ba contamination, surface preparation and LITD power may account for large variation in the amount of Ba recovered. We do not have a satisfactory explanation for this wide variation in results from these substrates.

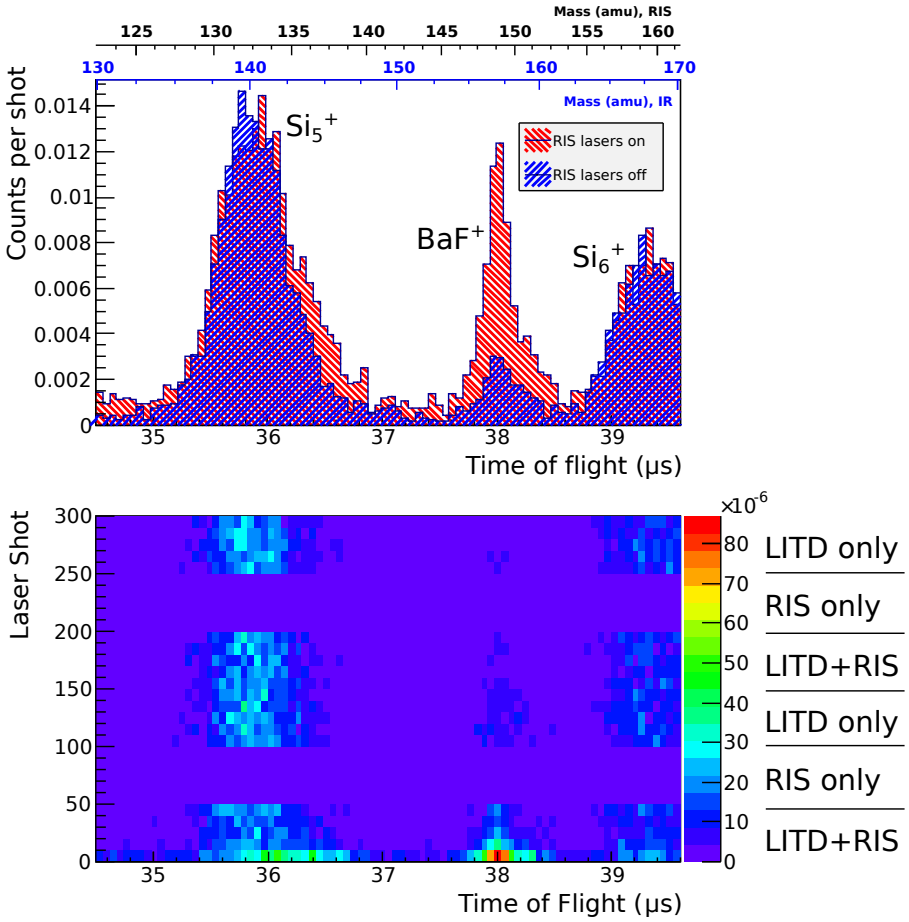

Figure 4.18: RIS laser dependence of deposited BaF^+ peak on Si (111). The comparison of before and after deposit is shown in Figure 4.17. Because the lasers cycled every 50 shots, quickly decaying directly ionized peaks such as the BaF^+ peak appear much larger in the red histogram. It was not clear if the shoulder on the right hand side of the Si_5^+ peak is truly RIS dependent since it decayed in the first few shots. In other tests, such as those shown in Figures 4.15 and 4.19, the peak at this time of flight did not depend upon the RIS lasers, thus this was not interpreted to be RIS Ba^+.

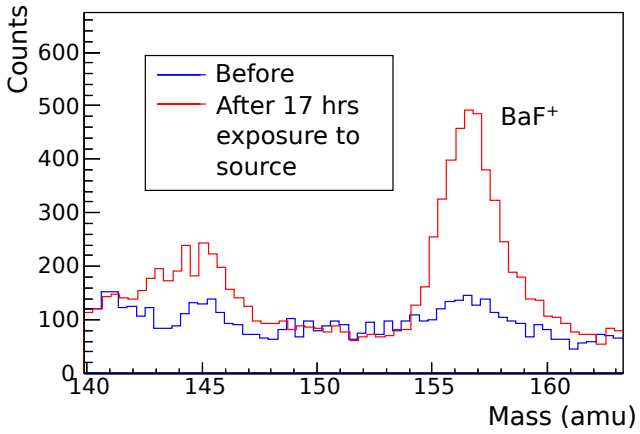

Figure 4.19: Deposited BaF^+ peak on the W substrate deposited on a Si wafer. The blue data show the TOF in the region of interest before exposure to the source, the red data show an identical scan after 17 hours exposure to the Gd-driven source.

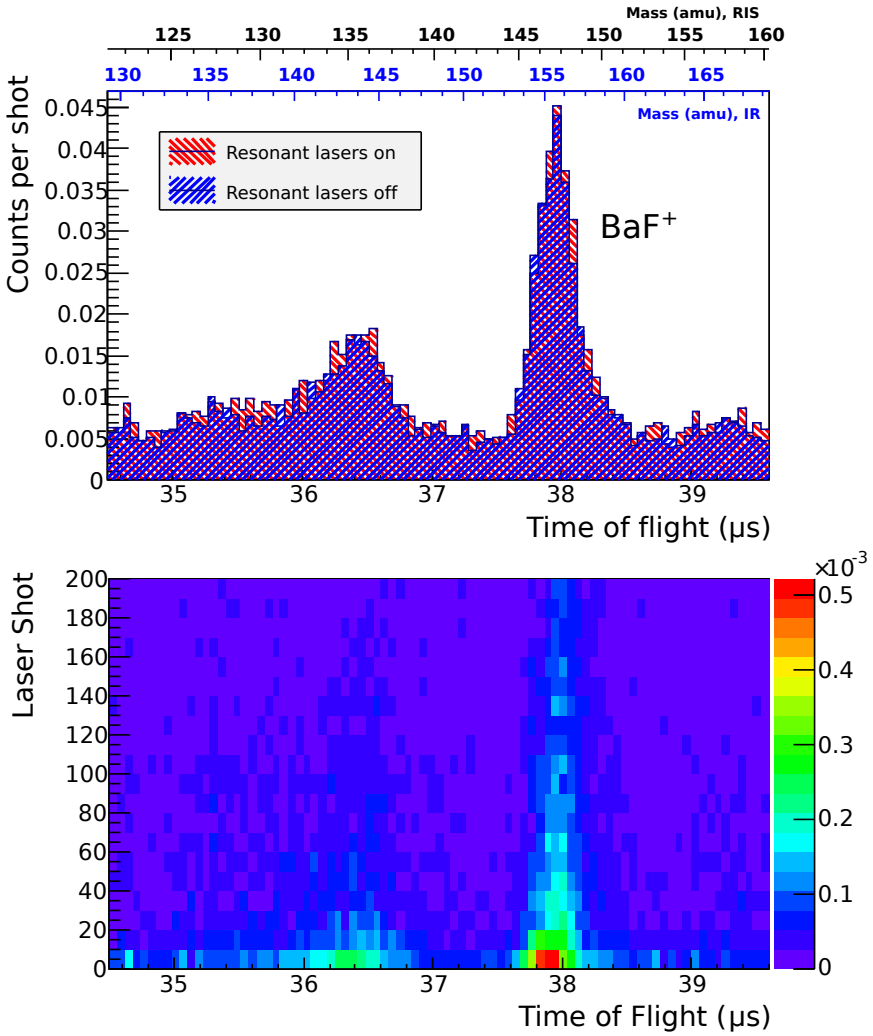

Figure 4.20: RIS laser dependence of deposited BaF^+ peak on the W substrate deposited on a Si wafer. This dataset takes advantage of cycling the RIS lasers on and off every other shot, which reduces the effect of performing the LITD+RIS cycle first (which likely led to the apparent RIS excess in this peak shown in Figure 4.18). This shows that the 144 amu/e peak was not dependent upon the RIS lasers.

Chapter 5

Cleaning Procedures

In order to maximize the efficiency of the LITD+RIS process, the surface must have chemical properties conducive to desorption and be free of contaminants that could form molecules with Ba or produce backgrounds in the signal region. There are a number of cleaning and surface preparation techniques that can help create these conditions, depending on the substrate used. This chapter focuses on techniques to clean substrates inside the vacuum system so that Ba can be deposited immediately after cleaning. In each procedure described, a control dataset was taken before cleaning, then the substrate was cleaned, and then a repeat of the initial dataset was taken again. This provided a measure of how each cleaning procedure changes the TOF spectrum.

The base vacuum pressure in this system—1×10^{-7} Torr in the RIS chamber—was not low enough to prevent adsorption of residual gases such as O_2, H_2O, CO_2, and CO over several minutes, potentially erasing the effects of these cleaning techniques. If these gases reacted with Ba on the surface then the efficiency of Ba recovery would have been reduced. Future efforts to improve the vacuum may improve the sensitivity.

5.1 Laser Cleaning

Because LITD removes adatoms, it is an effective technique to clean the surface of impurities. In this system, this was achieved by rastering the LITD laser across the

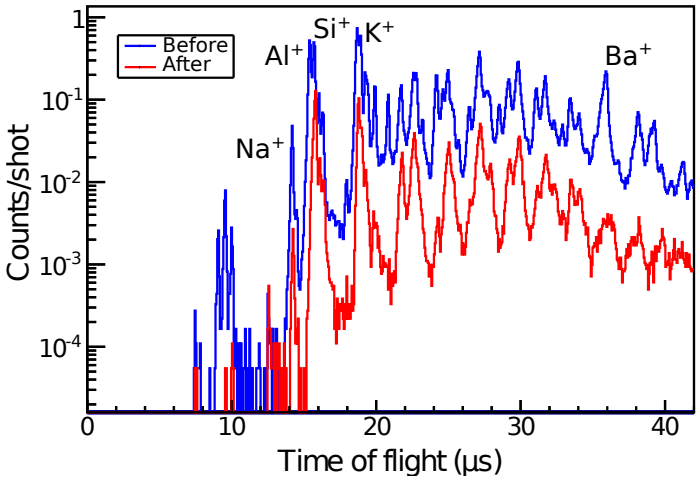

Figure 5.1: Laser cleaning of 6H-SiC (0001). Rastering the IR laser across the substrate is an effective cleaning technique. This TOF spectrum shows the reduction in counts at all times of flight after rastering across the 6H-SiC (0001) substrate with 1200 pulses per location at 2.6 MW/cm^2.

substrate. Since LITD heats the surface only locally[1], it prevents diffusion of ions out of the bulk material. Cleaning scans used more laser pulses at higher pulse energies than scans used to measure the surface cleanliness.

The effect of laser cleaning is shown in Figure 5.1. This shows two identical scans of a 6H-SiC (0001) substrate using 200 shots at each location with an LITD peak intensity of 1.6 MW/cm^2, separated by a cleaning scan (1200 pulses at a peak intensity of 2.6 MW/cm^2). These scans did not use the RIS lasers. Due to this laser cleaning scan, backgrounds at all times of flight were reduced. Note that there was a significant reduction in the directly ionized Ba^+ peak, although it was not eliminated. Elimination of this Ba contamination is necessary to detect deposition of small numbers of Ba^+ atoms.

This cleaning process was the primary cleaning technique used in this system because rastering the laser across the substrate always reduces backgrounds to the signal in the Ba^+ region of interest. Despite the overall reduction in ion counts, the K^+ peak appeared to decrease at a slower rate than the Ba^+ peak. Increasing the

[1]The temperature rise at a depth of 3 μm is less than 10% of the surface temperature rise in the heavily doped Si case described in Section 2.2.

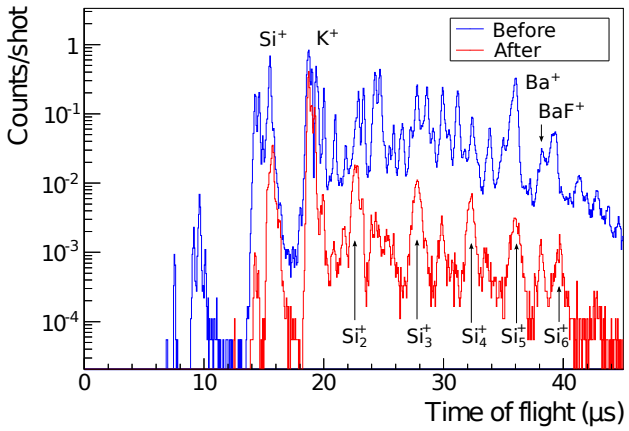

Figure 5.2: Laser cleaning of a heavily doped Si (100) substrate. This shows the reduction in most backgrounds with the exception of Si_n^+ peaks and a small amount of BaF^+.

LITD laser pulse energy helped remove adatoms, but higher intensities risk damaging the surface through ablation or substrate melting. The background reduction due to laser cleaning on Si (100), including evidence of Si_n^+ clusters after cleaning, is shown in Figure 5.2. Identical raster scans of the substrate using 200 shots/position and 1.5 MW/cm^2 LITD pulses were repeated before and after a laser cleaning scan. The laser cleaning scan used 2.3 MW/cm^2 LITD pulses, with 1200 shots per location. The efficacy of the cleaning is again shown by the reduction in the total number of counts in the TOF, although also in this case a significant K^+ peak remained. While the cleaning scan greatly reduced the amount of Ba^+ directly ionized by the LITD laser, the Si_5^+ (140 amu/e) peak may have obscured a small amount of remaining Ba^+. Laser cleaning in this case reduced but did not completely eliminate the BaF^+ peak present prior to the cleaning scan. Careful adjustment of the laser power allowed removal of contaminants including Ba without surface damage that could lead to Si_n^+ peaks.

Laser cleaning has also been applied to Ta substrates, shown in Figure 5.3. In this case, the LITD laser was rastered across the substrate with a peak intensity of 0.49 MW/cm^2. Then the substrate was cleaned with 300 pulses at each location with an intensity of 1.6 MW/cm^2. Finally, the same initial scan was repeated, confirming

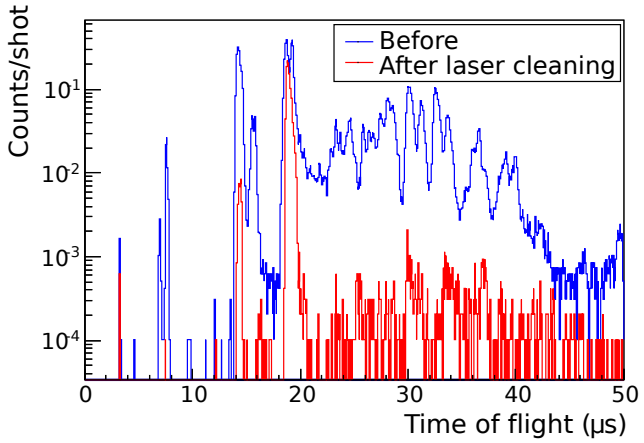

Figure 5.3: Laser cleaning of a Ta substrate. The blue histogram shows a scan before laser cleaning, while the red histogram shows the same scan after laser cleaning. The remaining peak at 37 μs was interpreted to be RIS Ba^+, however the background was greatly reduced.

a large reduction in the backgrounds in the region of interest, with the exception of a small peak at 37 μs, which may have been residual RIS Ba^+. This cleaning technique was able to reduce the number of counts in the signal region.

5.2 Resistive Heating

Resistive heating cleans heavily doped Si and SiC by thermally desorbing contaminants from the surface [82]. Not only can resistive heating remove contaminants, but it can also restructure the surface atoms, reducing the reactivity of the surface [27]. A common technique used to produce atomically clean Si surfaces heats the substrate for several hours at 650°C to outgas contaminants, then removes the oxide layer by heating to 1250°C for 1-2 minutes [63]. We sought to reproduce this cleaning scheme in our system.

Results of heating a heavily doped Si (100) substrate are shown in Figure 5.4. Scans were performed before and after heating to 700°C for 1 hour then ramping up to 1050°C over less than 1 minute[2]. Most peaks in the TOF spectrum did not

[2]Electrical connectivity problems at high temperatures prevented us from reaching the prescribed

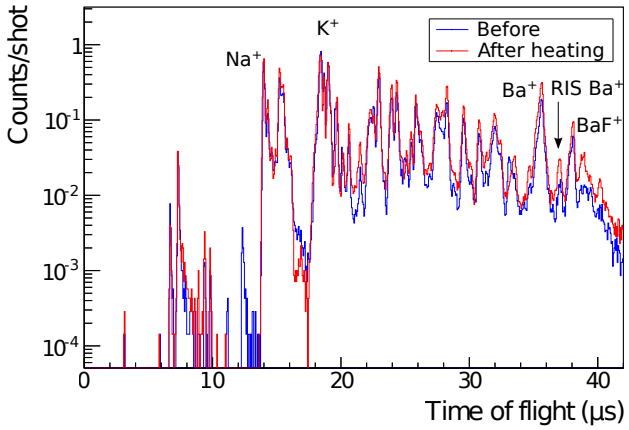

Figure 5.4: TOF spectrum before and after resistive heating cleaning of a heavily doped Si (100) substrate. The cleaning procedure involved heating for 1 hour at 700°C and then increasing to 1050°C for 30 seconds to remove oxides. After heating there is slightly more Ba^+ and BaF^+, and RIS Ba^+.

decrease, and the Ba^+, RIS Ba^+, and BaF^+ peaks were slightly larger after heating. This increase in Ba peaks from heating has been seen on Si (100) and (111), and appeared even if the substrate had not been exposed to the Ba source.

Heating for long periods in the range of 950°C to 1250°C causes micron scale damage to the surface [83], as shown on one substrate that had been heated for long periods in this range (Figure 5.5). The heavily doped Si (100) substrate was heated to 1000°C for several hours. Evidence of this surface damage appeared in the TOF as Si_n^+ clusters (Figure 5.6).

Literature does not agree on whether resistive heating should be sufficient to remove Ba from Si substrates. Some studies have shown that resistive heating is not capable of removing all Ba from a Si (100) [64] or a Si (111) substrate [65]. In these studies, authors were unable to recover Low-Energy Electron Diffraction (LEED) evidence of the expected clean surface reconstructions even after heating the substrate at length. Both experiments were able to recover the expected signal of clean Si substrates using Ar^+ ion sputtering. In conflict with these studies, others claim that resistive heating to 1200°C recovers the LEED signal indicative of a clean

temperature of 1250°C.

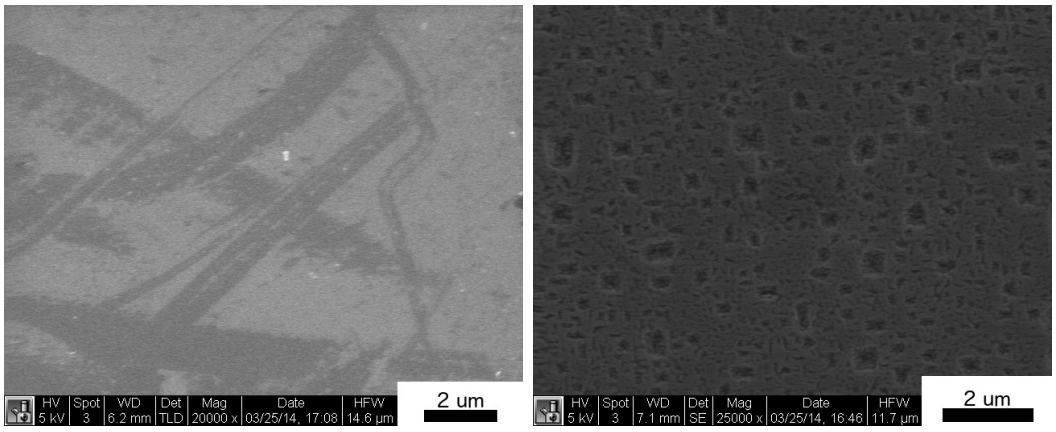

Figure 5.5: SEM image of 1 µm-scale surface damage on heavily doped Si (100) due to heating. The image on the left shows an unheated sample, while the image on the right shows a sample after heating to around 1000°C for several hours.

Si (100) surface [69]. In our experiment, heating did not eliminate Na^+, K^+ and Ba^+ backgrounds from the TOF spectrum, and in many cases increased these backgrounds.

We also used resistive heating to clean a W layer deposited on a Si wafer (Results from this substrate are discussed in Sections 4.1.2 and 4.3. The effect of heating a W substrate is shown in Figure 5.7. In this test, LITD+RIS prior to heating the W substrate showed evidence of directly ionized BaF^+ at 38 µs. After heating, this peak was absent, and backgrounds in the region of interest had been greatly reduced. This heating did however increase the directly ionized Rb^+ and Cs^+ peaks (at 28 µs and 35 µs, respectively). This reduction in backgrounds in the region of interest contrasted the results from Si substrates, and suggests that this was an effective technique for cleaning the W substrate. Attempts to heat a W substrate using an electron gun before this W-on-Si substrate was procured are detailed in the following section.

5.3 Heating Using an Electron Gun

Heating W and Ta substrates to near their melting points is one component of preparing these substrates [82], however the temperatures required for the prescribed preparation of these substrates are above the maximum sustained by the mounting systems

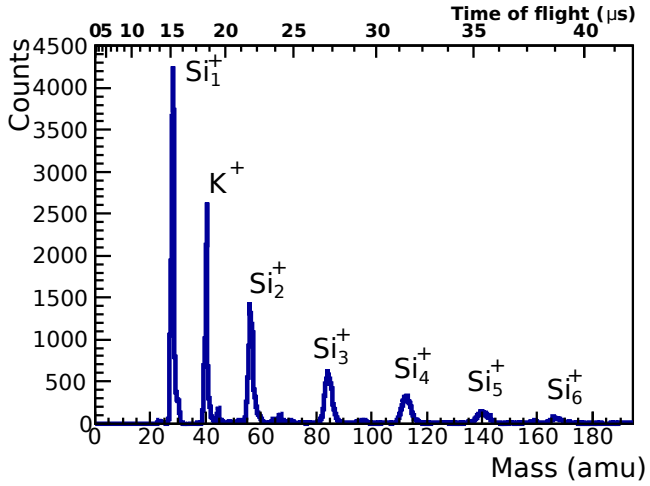

Figure 5.6: Si_n^+ clusters directly ionized from the heavily doped Si (111) substrate.

used. These metal substrates were mounted as shown in Figure 3.7A, where temperatures are limited by the maximum operating temperature of Macor (1000°C, [84]), well below the melting points of W and Ta (3683 K and 3269 K, respectively). Preparation of atomically clean Ni substrates described in [82] requires sputtering using an Ar^+ ion gun in addition to heating to $700 - 1000$°C. Our system does not have an ion gun to sputter these substrates. In spite of the fact that [82] suggests that heating to 1000°C alone is not sufficient to clean these substrates, it was tested for W, Ta and Ni.

Thoriated W filaments heated to ~ 1500°C served as electron guns in these tests. The substrate was positioned 1 cm from the filament and was biased to +1.5 kV to draw electrons to the substrate. The substrate was heated by the current of electrons impinging on the surface, typically around 1 mA with a potential difference of 1 kV. Figure 5.8 shows a picture of the hot filament and heated substrate.

A Ta substrate was heated to about 1100°C for 5 minutes[3]. A comparison of before and after electron gun heating on this Ta substrate is shown in Figure 5.9. The initial scan of 400 LITD shots/location at a peak intensity of 0.49 MW/cm^2 showed only K^+ ions. After electron gun heating, the Na^+ peak appeared, the K^+ peak increased,

[3]While this temperature is above the maximum service temperature of the Macor support, the substrate remained in place during heating.

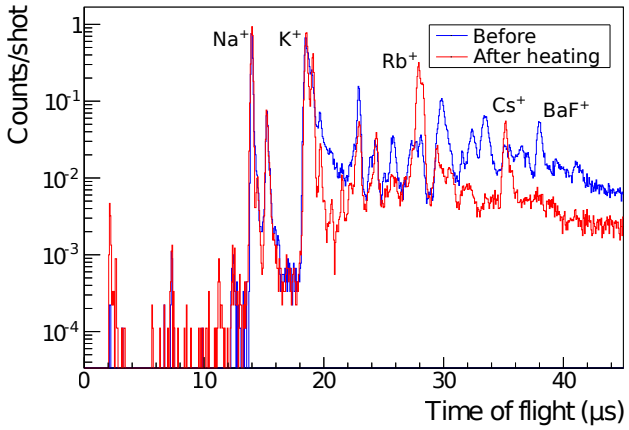

Figure 5.7: Cleaning using resistive heating of a W substrate. Most peaks, including BaF^+ decrease after heating at 700°C for an hour then 10 seconds at 1100°C. Alkali peaks such as Rb^+ and Cs^+ increase after the heating.

and several other background peaks increased. This heating produced a small peak of RIS Ba^+. In this configuration, the electrons impinged on the front of the substrate, which may have unintentionally deposited atoms from the hot filament. However, tests in which the filament was heated but the substrate was not showed no increase in Ba backgrounds. Because this heating technique increased contaminations, it is no longer used.

5.4 Hydrogen Glow Discharge

Hydrogen passivation limits the reactivity of Si substrates by occupying dangling surface Si bonds with H atoms [27]. This adsorbed monolayer of H atoms prevents oxidation of Si substrates but allows adsorption of Ba. However, the presence of asorbed H can form of BaH_2 molecules upon desorption [85], a potential complication for RIS of Ba. A separate study using STM found that the Ba diffusion increased across the surface [86]. H passivation was of interest because of its ability to prevent surface oxidation.

For passivation and cleaning *in situ*, the RIS chamber was filled with H_2 gas.

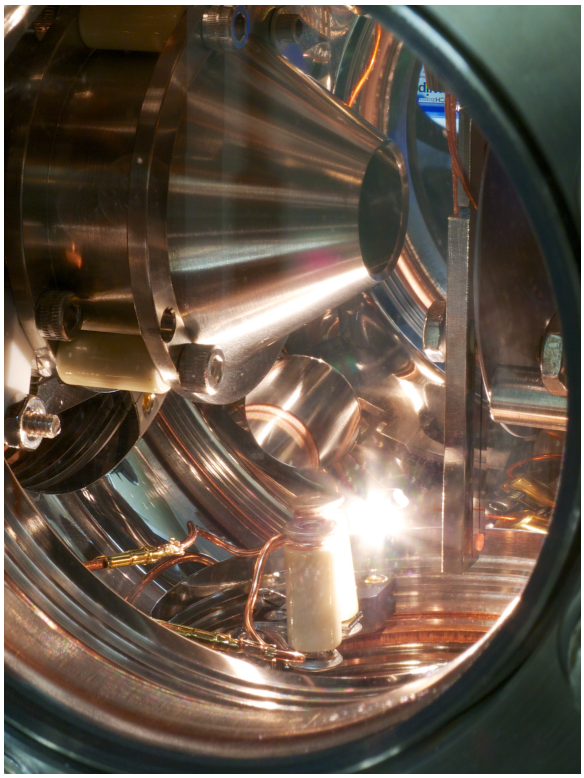

Figure 5.8: Heating the substrate with electron gun. Note the substrate, mounted on the end of the probe, glowing orange-red.

Molecular H_2 does not adsorb on Si substrates, so H_2 must be converted to atomic H [85, 86]. We used a glow discharge between a Ti electrode and the substrate, which had been shown to clean and H-passivate surfaces [87]. The substrate was biased to -230 V while the electrode ($\sim$ 1 cm from the substrate) was biased to +1000 V. This started a glow discharge in roughly 1 Torr (near the Paschen minimum) of H_2, which was then maintained for 40 minutes.

Figure 5.10 shows large increase in backgrounds from a heavily doped Si (111) substrate after this cleaning cycle followed by 1 hour exposure to the Gd-driven Ba source. The scans before and after the H discharge used 200 LITD shots per location with a peak intensity of 1.4 MW/cm^2. This showed a significant increase in the BaF^+ peak at 37.5 µs, but no increase in an RIS Ba^+ peak. Si_n^+ peaks remained relatively unchanged. While the increase in BaF^+ may have been due to exposure to the source,

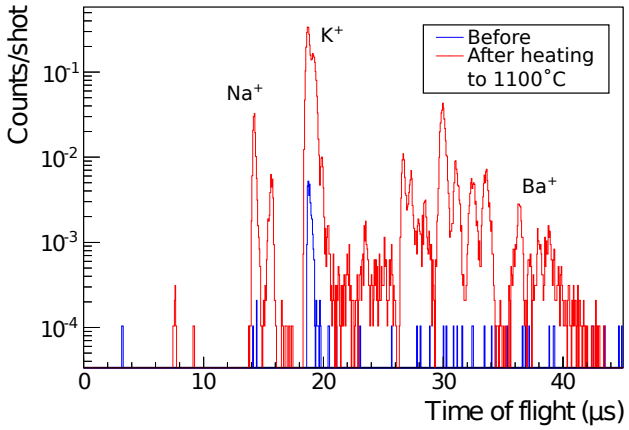

Figure 5.9: TOF spectrum before and after electron gun heating of a Ta substrate. The substrate was heated to about 1100°C for 5 minutes. The total number of counts increased overall, including a very small amount of Ba.

it is clear that this surface preparation technique led to large increases in background and thus was not pursued further.

5.5 Summary of Cleaning Techniques

The results of these cleaning techniques showed that substrate cleaning is nontrivial but necessary for eliminating the backgrounds in the signal region of interest. Laser cleaning was found to be the most effective cleaning technique used and was the most commonly used in this system. Results of attempts to detect Ba deposited from the Gd-driven source after laser cleaning produced BaF^+ but not RIS Ba^+, as described in Section 4.3. Since other techniques described increased backgrounds they are no longer used. None of the techniques tested removed all surface contaminants; thus cleaning and preparation remains the subject of ongoing research.

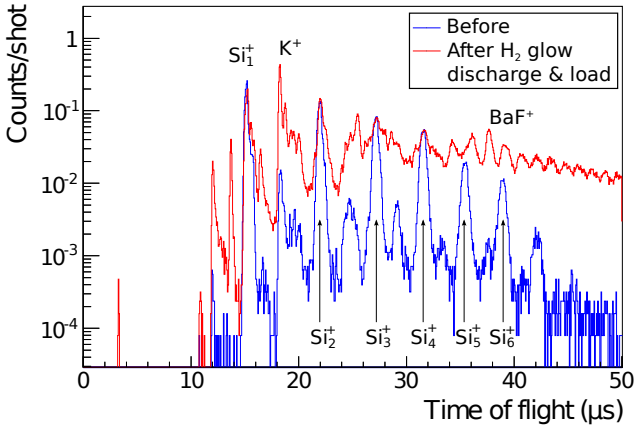

Figure 5.10: Effect of 40 minutes H_2 glow discharge followed by 1 hour exposure to the Gd-driven Ba source on a heavily doped Si (111) substrate. The BaF^+ peak at 37.5 μs increased due to this combined action, as well as the overall background counts.

Chapter 6

Ongoing Efforts

The detection of Ba from many substrates is a successful step forward in Ba tagging, but two major challenges remain. The first challenge is to reduce the background due to Ba present on the surface. While it appears that laser cleaning can remove most traces of Ba from the TOF, the detection of individual Ba ions from $0\nu\beta\beta$ requires an exceedingly low chance for a false positive, still well below the level we have been obtaining on various substrates. The second challenge is to measure and improve Ba transport and identification. While BaF^+ has been recovered from deposits using the Gd-driven source, the deposit and recovery of Ba through the selective RIS process has not been confirmed, indicating that molecule formation may impede our efforts to detect Ba atoms on the surface. This improvement may require trying new substrates that have not yet been tested in our system, or possibly modifying the concept of Ba tagging to retrieve and identify Ba molecules.

6.1 Substrate Selection and Cleaning

Substrates with the appropriate adsorption and desorption properties remain under investigation. The substrates tested have shown some Ba signals, primarily from Ba contamination, however Si and W have shown BaF^+ peaks from about 15 hours of exposure to the Gd-driven source. While tests of Ba deposit were conducted on the Ta, Ni and SiC substrates, these tests were limited to about 1 hour, rather than the

overnight deposit that produced BaF^+ peaks from Si and W. This test should be conducted also on the Ta, Ni and SiC substrates for comparison to the results from Si and W.

Tests using the graphinated SiC substrate showed that Ba can be desorbed and ionized, however the material used in this case had a significant Ba contamination. Furthermore, simulations of Ba adsorption on graphene have shown that the desorption energy could be relatively low [43]. While heteroepitaxial graphene from SiC is relatively easy to grow, this material may have bulk Ba contamination. Graphene may be cleaner if grown using Chemical Vapor Deposition (CVD), a process that deposits clean layers of graphene on top of a substrate using methane gas [88]. A graphene surface could be prepared inside the vacuum system immediately before attempting to recover Ba. This preparation could help limit adsorption of unwanted impurities. Initial tests of CVD graphene would use a separate commercial system to deposit graphene. If tests of CVD graphene prepared outside the vacuum system show that CVD graphene is promising, then it would be relatively easy to prepare CVD graphene inside this system. This would require the addition of a system to deliver the methane gas required to grow the graphene.

In order to ensure that surfaces remain clean, the vacuum pressure in the system must be reduced significantly from the current base pressure of 1×10^{-7} Torr. At this pressure one monolayer of residual gases in the vacuum system adsorbs in a matter of a few seconds [27]. These gases may react with adsorbed Ba to form molecules which would impede detection of the ions through RIS. The goal is to reduce the pressure to Ultra High Vacuum (UHV, $< 10^{-9}$ Torr), a typical pressure for surface science experiments [27]. Pump technologies under consideration for reducing the pressure to this level are ion pumps and Non-Evaporable Getter (NEG) pumps. These pumps could be used individually or together.

Ongoing work is focused on the cleanliness of all substrates. Initial Ba contaminations are large enough to obscure any depositions of Ba from the ion source, but Ba backgrounds were successfully eliminated from the TOF using laser cleaning. Further cleaning techniques could help eliminate Ba as well as potential reactants from the surface.

Ar^+ ion sputtering may be a useful addition to the current list of cleaning techniques. Experiments using Ba on Si surfaces showed that prolonged heating may not remove Ba from Si substrates, requiring sputtering with an Ar^+ ion gun to remove the last traces of Ba [64]. Installation of an Ar^+ ion gun in this system would add yet another proven effective cleaning technique, which may reduce surface contamination to the required level. For some substrates, the standard cleaning techniques require sputtering. For example, preparation of atomically clean W and Ni substrates requires the use of argon ion sputtering [82]. Sputtering may be effective for cleaning Ta as well.

6.2 Loading in Gas Xenon

In tests of Ba deposit using the Gd-driven Ba source, only BaF^+ was detected. While the Gd-driven source is known to emit BaF^+ [54], the ^{252}Cf fission source will not produce F. We would like to test recovery in the absence of F using the ^{252}Cf source, which requires using gas or liquid Xe to stop the relatively high-energy fission products. Because liquid xenon requires the additional step of cooling the cell, it is easier to initially test this source in Xe gas. While the Ba emission from the 1 kBq ^{252}Cf fission source we procured for this application is 10× lower than the Ba emission of our Gd-driven source, it should be possible to initially detect an increase in the Ba from a 15 hour deposit.

Tests using gas Xe would also represent a step toward liquid Xe, the final medium to be used in the detector, in this case assumed to be liquid Xe. The comparison of Ba adsorption in vacuum and in Xe has not been measured, although the effect of Xe (gas or liquid) on how the Ba adsorbs to the surface is assumed to be minimal because of the inert nature of Xe. Even so, because the final application requires recovery of Ba from a LXe detector, this experiment must ultimately characterize Ba recovery from LXe.

6.3 *Ab initio* Calculations of Adsorption

Computational methods for evaluating substrates may help explain the adsorption and desorption of Ba from various surfaces. The strength of adsorption bonds can be calculated using *Ab initio* methods. These calculations seek to estimate the strengths and parameters of chemical interactions through a variational approximation of the many-body Schrödinger equation. This technique has successfully modeled substrates of many different materials [27, 40, 43, 89]. Furthermore, these calculations can be applied to understand the type of bond between the surface and the substrate, since in ionic bonding some charge will be transferred from the adatom to the substrate, *ab initio* calculations can report this transfer. Understanding the capability and drawbacks of this technique can aid in constructing computational models of Ba adsorption on surfaces. An *ab initio* study could help select substrates.

Typical *ab initio* calculations of substrate binding energies use collections of a few tens of atoms arranged in the appropriate surface structure with periodic boundary conditions called a *supercell*. A typical supercell models a few unit cells of surface with a depth of about 5 atomic layers separated by a layer of vacuum. This depth gives enough of the bulk structure to provide an estimation of how an adsorbate will bind to the substrate, while only requiring modest computational resources [40]. Since the supercell surface is several unit cells in area, a single adatom per supercell models a low surface coverage with minimal interactions between adatoms.

Adsorption energies are computed using three different calculations: the surface alone (E_{surface}), the adsorbate alone (E_{adatom}) and finally the combined substrate-adsorbate system ($E_{\text{surface+adatom}}$) [43]. The adsorption energy is:

$$E_{\text{ads}} = E_{\text{surface+adatom}} - E_{\text{surface}} - E_{\text{adatom}}. \tag{6.1}$$

A preliminary example of this type of calculation is shown in Figure 6.1. This computation uses the PWSCF package [90] with the density functional described in [91]. The supercell in this case consists of 21 C atoms in a single layer, with the Ba adatom above a graphene ring, as shown in Figure 6.2. The electron cutoff energy is 4.1 keV, with a k point mesh of $8 \times 8 \times 1$. The potential varies as the distance above a

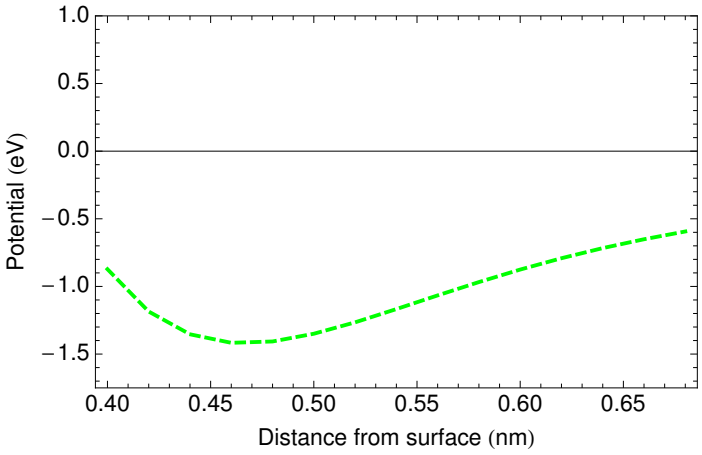

Figure 6.1: Barium adsorption potential above a graphene ring site as the distance between the graphene and adatom is varied. An illustration of the supercell used is shown in Figure 6.2.

single graphene monolayer is varied. The minimum potential is at 0.46 nm from the monolayer, with a bond strength of 1.42 eV. These results are slightly different from those obtained in [43], which claim a separation of 0.249 nm with a bond energy of 0.67 eV.

Further work should focus on ensuring that the computational parameters are correct. Additionally, graphene surfaces are generally simulated as a single layer of atoms, however a practical application of graphene for Ba tagging will use graphene adsorbed on some substrate, which may in turn affect adsorption of Ba on the outside of the substrate. These simulations also must include displacement of the substrate atoms, which this simulation does not. Simulations on Si [41, 42] and graphene [43] allow for movement of the substrate atoms in the vicinity of the adsorbed Ba.

Investigations of other surfaces could reveal other potential substrates for this experiment. However, each calculation must be experimentally verified because large errors in desorption energies can persist in the calculation [40].

It may be possible to measure the E_{des} of Ba on graphitized SiC using radioactive beam sources. Our collaborators have succeeded in measuring the desorption of ^{139}Ba from a heated Ta substrate [92]. In this case, the ^{139}Ba is deposited on the substrate while the substrate has a frozen layer of Xe on the surface. The layer of Xe is then

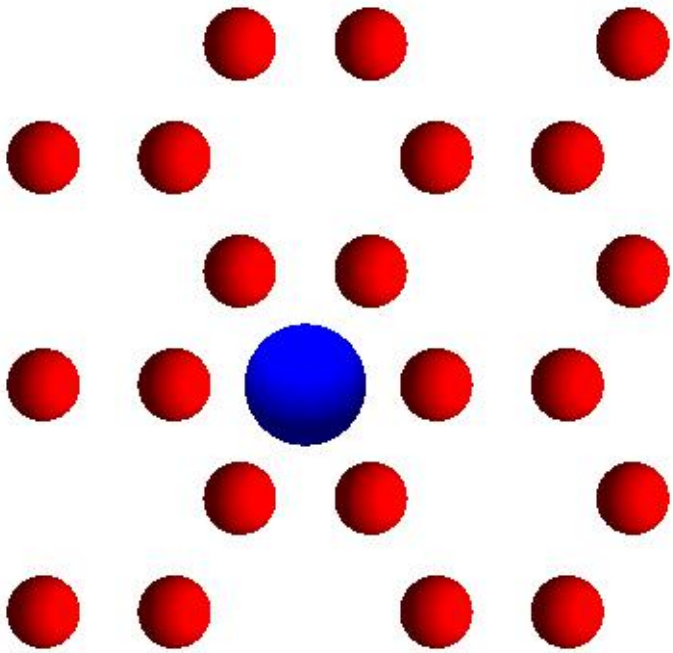

Figure 6.2: Illustration of the supercell used for *ab initio* calculation. The red spheres represent carbon atoms, while the blue sphere represents the Ba adatom.

removed, and the substrate is moved in front of a Ge detector to measure decays of the ^{139}Ba. The substrate is then heated to desorb the Ba, then moved away. If ^{139}Ba decays are still measured, then Ba has successfully been desorbed from the surface. It was found that the Ba desorbs as a neutral atom, not as an ion. This system may be of use in determining which surfaces are best for thermal desorption, and therefore which surfaces may be worth trying in the RIS system.

Bibliography

[1] J. Beringer, et al. Review of Particle Physics. *Physical Review D*, 86(1):010001, July 2012.

[2] F. Avignone, S. R. Elliott, and J. Engel. Double beta decay, Majorana neutrinos, and neutrino mass. *Reviews of Modern Physics*, 80(2):481–516, April 2008.

[3] B. Kayser. Neutrino Mass, Mixing, and Flavor Change. In *Neutrino Mass*, pages 1–24. Springer Berlin Heidelberg, Berlin, Heidelberg, September 2003.

[4] D. V. Forero. Global status of neutrino oscillation parameters after Neutrino-2012. *Physical Review D*, 86(7):073012, October 2012.

[5] E. W. Otten and C. Weinheimer. Neutrino mass limit from tritium β decay. *Reports on progress in physics*, 71(8):086201, July 2008.

[6] Planck Collaboration. Planck 2013 results. XVI. Cosmological parameters. *arXiv preprint astro-ph/0410296*, March 2014.

[7] A. De Gouvea. Neutrinos Have Mass—So What? *Modern Physics Letters A*, 19(38):2799–2813, 2004.

[8] B. Kayser, F. Gibrat-Debu, and F. Perrier. *The Physics of Massive Neutrinos*. World Scientific Lecture Notes in Physics. World Scientific, Singapore, July 1989.

[9] J. Barea and F. Iachello. Neutrinoless double-β decay in the microscopic interacting boson model. *Physical Review C*, 79(4):044301, 2009.

[10] J. Menéndez, A. Poves, E. Caurier, and F. Nowacki. Disassembling the nuclear matrix elements of the neutrinoless $\beta\beta$ decay. *Nuclear Physics A*, 818(3-4):139–151, March 2009.

[11] A. Staudt, K. Muto, and H. V. Klapdor-Kleingrothaus. Calculation of 2ν and 0ν Double-Beta Decay Rates. *Europhysics Letters*, 13(1):31–36, July 2007.

[12] T. R. Rodríguez and G. Martínez-Pinedo. Energy Density Functional Study of Nuclear Matrix Elements for Neutrinoless $\beta\beta$ Decay. *Physical Review Letters*, 105(25):252503, December 2010.

[13] M. Agostini, et al. Results on Neutrinoless Double-β Decay of ^{76}Ge from Phase I of the GERDA Experiment. *Physical Review Letters*, 111(12):122503, September 2013.

[14] J. B. Albert, et al. Search for Majorana neutrinos with the first two years of EXO-200 data. *Nature*, 510(7504):229–234, February 2014.

[15] A. Gando, et al. Limit on Neutrinoless $\beta\beta$ Decay of ^{136}Xe from the First Phase of KamLAND-Zen and Comparison with the Positive Claim in ^{76}Ge. *Physical Review Letters*, 110(6):062502, February 2013.

[16] H. V. Klapdor-Kleingrothaus, et al. Latest results from the Heidelberg-Moscow double beta decay experiment. *The European Physical Journal A-Hadrons and Nuclei*, 12(2):147–154, 2001.

[17] H. V. Klapdor-Kleingrothaus, A. Dietz, H. L. Harney, and I. V. Krivosheina. Evidence for Neutrinoless Double Beta Decay. *Modern Physics Letters A*, 16(37):2409–2420, December 2001.

[18] H. V. Klapdor-Kleingrothaus, I. V. Krivosheina, and S. N. Karpov. Why is the Conclusion of the GERDA Experiment Wrong? *arXiv.org*, August 2013.

[19] F. Šimkovic, A. Faessler, H. Müther, V. Rodin, and M. Stauf. $0\nu\beta\beta$-decay nuclear matrix elements with self-consistent short-range correlations. *Phys. Rev. C*, 79:055501, May 2009.

[20] D. Fancher, et al. Performance of a time-projection chamber. *Nuclear Instruments and Methods in Physics*, 161(3):383–390, 1979.

[21] M. Auger, et al. The EXO-200 detector, part I: detector design and construction. *Journal of Instrumentation*, 7(05):P05010, 2012.

[22] N. Ackerman, et al. Observation of Two-Neutrino Double-Beta Decay in ^{136}Xe with the EXO-200 Detector. *Physical Review Letters*, 107(21):212501, 2011.

[23] J. B. Albert, et al. Improved measurement of the $2\nu\beta\beta$ half-life of ^{136}Xe with the EXO-200 detector. *Physical Review C*, 89(1):015502, January 2014.

[24] M. K. Moe. Detection of neutrinoless double-beta decay. *Physical Review C*, 44(3):R931–R934, 1991.

[25] M. Green, et al. Observation of single collisionally cooled trapped ions in a buffer gas. *Physical Review A*, 76(2):023404, 2007.

[26] H. Dehmelt. Radiofrequency Spectroscopy of Stored Ions I: Storage. In R. B. Bates and I. Estermann, editors, *Advances in Atomic & Molecular Physics*, page 53. Academic Press, June 1969.

[27] K. Oura, V. G. Lifshits, A. Saranin, and A. V. Zotov. *Surface Science: An Introduction*. Springer, Berlin, New York, July 2003.

[28] A. H. A. Lutey. An improved model for nanosecond pulsed laser ablation of metals. *Journal of Applied Physics*, 114(8):083108, 2013.

[29] D. Marla, U. V. Bhandarkar, and S. S. Joshi. A model of laser ablation with temperature-dependent material properties, vaporization, phase explosion and plasma shielding. *Applied Physics A*, November 2013.

[30] G. S. Hurst, M. G. Payne, S. D. Kramer, and J. P. Young. Resonance ionization spectroscopy and one-atom detection. *Reviews of Modern Physics*, 51(4):767, 1979.

[31] J. Blewett and E. Jones. Filament Sources of Positive Ions. *Physical Review*, 50(5):464–468, September 1936.

[32] T. L. Tan, Z. L. Zhou, and P. P. Ong. Oxides as thermionic sources of Mg^+, Ca^+, Sr^+, and Ba^+ ions. *Review of Scientific Instruments*, 66(4):2879–2882, 1995.

[33] H. Lüth. *Solid Surfaces, Interfaces and Thin Films*. Springer, September 2010.

[34] S. Hongo, K. Ojima, S. Taniguchi, T. Urano, and T. Kanaji. Observation of the interface of Ba/Si (100) by MDS and TDS. *Applied surface science*, 82:537–542, 1994.

[35] A. Shih, J. E. Yater, and R. Abrams. Thermal desorption of Ba from tungsten. *Applied surface science*, 146(1):1–6, 1999.

[36] D. Vlachos, S. D. Foulias, S. Kennou, C. Pappas, and C. Papageorgopoulos. Ba deposition on Ni (110). *Surface science*, 331:673–678, 1995.

[37] U. van Slooten, W. R. Koppers, A. Bot, H. M. van Pinxteren, A. M. C. Moutinho, J. W. M. Frenken, and A. W. Kleyn. The adsorption of Ba on Ag(111). *Journal of Physics: Condensed Matter*, 5(31):5411–5428, January 1993.

[38] G. G. Magera and P. R. Davis. Cesium and barium adsorption onto a clean niobium (110) surface. *AIP Conf. Proc.*, 271(3):1633–1638, 2008.

[39] P. A. Redhead. Thermal desorption of gases. *Vacuum*, 12(4):203–211, 1962.

[40] D. S. Sholl and J. A. Steckel. *Density Functional Theory*. John Wiley & Sons, Inc., Hoboken, NJ, USA, March 2009.

[41] J. Wang, J. A. Hallmark, D. S. Marshall, W. J. Ooms, P. Ordejón, J. Junquera, D. Sánchez-Portal, E. Artacho, and J. M. Soler. Bonding and diffusion of Ba on a Si (001) reconstructed surface. *Physical Review B*, 60(7):4968, 1999.

[42] Z. G. Wang and X. T. Zu. First principles calculations of adsorption and diffusion of Ba on a reconstructed Si (100) surface. *Surface Review and Letters*, 13:365–368, January 2006.

[43] K. Nakada and A. Ishii. Migration of adatom adsorption on graphene using DFT calculation. *Solid State Communications*, 151(1):13–16, January 2011.

[44] L. A. Hemstreet and S. R. Chubb. Electronic structure of $c(2 \times 2)$ Ba adsorbed on W (001). *Physical Review B*, 47(16):10748, 1993.

[45] J. Ready. *Effects of High-Power Laser Radiation*. Academic Press, June 1971.

[46] D. Burgess Jr, P. C. Stair, and E. Weitz. Calculations of the surface temperature rise and desorption temperature in laser-induced thermal desorption. *Journal of Vacuum Science & Technology A*, 4(3):1362–1366, 1986.

[47] G. E. Jellison. Optical absorption coefficient of silicon at 1.152 μ at elevated temperatures. *Applied Physics Letters*, 41(7):594, 1982.

[48] B. G. Koehler and S. M. George. Laser-induced desorption of H_2 from Si (111) 7×7. *Surface science*, 248(1):158–172, 1991.

[49] M. Montero Díez. *Development of a Resonance Ionization Spectroscopy Ion-Transport Probe for the Enriched Xenon Observatory*. PhD thesis, Stanford University, May 2012.

[50] H. J. Metcalf and P. van der Straten. *Laser Cooling and Trapping*. Springer, January 1999.

[51] J. J. Curry. Compilation of Wavelengths, Energy Levels, and Transition Probabilities for Ba I and Ba II. *Journal of Physical and Chemical Reference Data*, 33(3):725–746, 2004.

[52] U. Fano. Effects of Configuration Interaction on Intensities and Phase Shifts. *Physical Review*, 124(6):1866–1878, December 1961.

[53] M. A. Kalyar, M. Rafiq, and M. A. Baig. Absolute photoionization cross section from the 6s6p $^{1,3}P_1$ excited states of barium. *Journal of Physics B: Atomic, Molecular and Optical Physics*, 40(12):2307, 2007.

[54] M. Montero Díez, et al. A simple radionuclide-driven single-ion source. *Review of Scientific Instruments*, 81(11):113301, 2010.

[55] G. Savard, S. Baker, C. Davids, A. F. Levand, E. F. Moore, R. C. Pardo, R. Vondrasek, B. J. Zabransky, and G. Zinkann. Radioactive beams from gas catchers: The CARIBU facility. *Nuclear Instruments and Methods in Physics Research Section B: Beam Interactions with Materials and Atoms*, 266(19):4086–4091, 2008.

[56] J. F. Ziegler, M. D. Ziegler, and J. P. Biersack. SRIM–The stopping and range of ions in matter (2010). *Nuclear Instruments and Methods in Physics Research Section B: Beam Interactions with Materials and Atoms*, 268(11):1818–1823, 2010.

[57] National Nuclear Data Center, information extracted from the Chart of Nuclides database, http://www.nndc.bnl.gov/chart/. (June 2014).

[58] T. R. England and B. F. Rider. Evaluation and compilation of fission product yields 1993. Technical report, Los Alamos National Laboratory (LANL), Los Alamos, NM, December 1995.

[59] B. Willke and M. Kock. Measurement of photoionization cross sections from the laser-excited Ba I (6s6p) $^1P_1^0$ state. *Journal of Physics B: Atomic, Molecular and Optical Physics*, 26(6):1129, 1993.

[60] P. Camus, M. Dieulin, A. El Himdy, and M. Aymar. Two-Step Optogalvanic Spectroscopy of Neutral Barium: Observation and Interpretation of the Even Levels Above the 6s Ionization Limit Between 5.2 and 7 eV. *Physica Scripta*, 27(2):125, 1983.

[61] D. A. Dahl. SIMION for the personal computer in reflection. *International Journal of Mass Spectrometry*, 200(1-3):3–25, December 2000.

[62] R. T. Short. High resolution time-of-flight spectrometry. *Physica Scripta*, 1997(T71):46, 1997.

[63] X. Hu, et al. Barium adsorption on Si (100) (2×1) at room temperature: a bipolar scanning tunneling microscopy study. *Surface science*, 457(1):L391–L396, 2000.

[64] D. S. Vlachos and C. A. Papageorgopoulos. Ba deposition on Si (100) 2×1. *Solid State Communications*, 90(3):175–181, 1994.

[65] H. H. Weitering. New barium-induced surface reconstructions on Si (111). *Surface science*, 355(1):L271–L277, 1996.

[66] W. C. Fan. Identification of ordered atomic structures of Ba on the Si (100) surface. *Surface science*, 253(1):297–302, 1991.

[67] T. Urano, K. Tamiya, K. Ojima, S. Hongo, and T. Kanaji. Adsorption structure of Ba on an Si(001)-(2×1) surface. *Surface science*, 357-358:459–463, June 1996.

[68] R. C. Estler and N. S. Nogar. Ablation of high-temperature superconductor studied by resonance ionization mass spectrometry (RIMS). *Journal of Applied Physics*, 69(3):1654–1659, 1991.

[69] Y. Takeda, T. Urano, T. Ohtani, K. Tamiya, and S. Hongo. Adsorption structure and silicide formation of Ba on the Si (001) surface. *Surface science*, 402:692–696, 1998.

[70] Y. Takeda, T. Ohtani, K. Ojima, T. Urano, and S. Hongo. UPS study of electronic states of Ba on Si (001) surface. *Journal of electron spectroscopy and related phenomena*, 88:619–624, 1998.

[71] C.-P. Cheng, I.-H. Hong, and T.-W. Pi. Synchrotron-radiation photoemission study of Ba on a Si (001) 2×1 surface. *Physical Review B*, 58(7):4066–4071, 1998.

[72] H. Boubekeur, J. Höpfner, T. Mikolajick, C. Dehm, L. Frey, and H. Ryssel. Aspects of Barium Contamination in High Dielectric Dynamic Random Access Memories. *Journal of The Electrochemical Society*, 147(11):4297, 2000.

[73] M. J. Pellin, C. E. Tripa, I. V. Veryovkin, W. F. Calaway, and A. M. Davis. Analyzing individual presolar grains with CHARISMA. *Geochimica et cosmochimica acta*, 67(17):3215–3225, 2003.

[74] M. R. Savina, A. M. Davis, C. E. Tripa, M. J. Pellin, R. S. Lewis, S. Amari, R. Gallino, and M. Lugaro. Barium isotopes in individual presolar silicon carbide grains from the Murchison meteorite. *Geochimica et cosmochimica acta*, 67(17):3201–3214, 2003.

[75] I. Forbeaux, J.-M. Themlin, and J.-M. Debever. Heteroepitaxial graphite on 6H-SiC (0001):Interface formation through conduction-band electronic structure. *Physical Review B*, 58(24):16396–16406, December 1998.

[76] I. Forbeaux, J.-M. Themlin, A. Charrier, F. Thibaudau, and J.-M. Debever. Solid-state graphitization mechanisms of silicon carbide 6H-SiC polar faces. *Applied surface science*, 162:406–412, 2000.

[77] K. Nakada and A. Ishii. DFT Calculation for Adatom Adsorption on Graphene. In *Graphene Simulation*, pages 1–19. InTech, August 2011.

[78] K. V. Emtsev, et al. Towards wafer-size graphene layers by atmospheric pressure graphitization of silicon carbide. *Nature Materials*, 8(3):203–207, February 2009.

[79] M. J. Dresser. The Saha-Langmuir Equation and its Application. *Journal of Applied Physics*, 39(1):338–339, 1968.

[80] R. Souda, W. Hayami, T. Aizawa, S. Otani, and Y. Ishizawa. Charge state of potassium on metal and semiconductor surfaces studied by low-energy D^+ scattering. *Physical Review Letters*, 69(1):192–195, July 1992.

[81] R. Souda, K. Yamamoto, W. Hayami, T. Aizawa, and Y. Ishizawa. Bond ionicity of alkaline-earth oxides studied by low-energy D^+ scattering. *Physical Review B*, 50(7):4733–4738, August 1994.

[82] R. G. Musket, W. McLean, C. A. Colmenares, D. M. Makowiecki, and W. J. Siekhaus. Preparation of atomically clean surfaces of selected elements: A review. *Applications of Surface Science*, 10(2):143–207, January 1982.

[83] B. S. Swartzentruber, Y. W. Mo, M. B. Webb, and M. G. Lagally. Scanning tunneling microscopy studies of structural disorder and steps on Si surfaces. *Journal of Vacuum Science & Technology A*, 7(4):2901–2905, 1989.

[84] Macor service temperature from www.professionalplastics.com/professionalplastics/content/downloads/Macor_Brochure_2014.pdf, accessed July 2014.

[85] D. S. Vlachos and C. A. Papageorgopoulos. Barium adsorption on hydrogenated Si (100) 2×1 surfaces. *Journal of Physics: Condensed Matter*, 8(45):8799, 1996.

[86] K. Ojima, M. Yoshimura, and K. Ueda. Effect of Hydrogen Termination on Ba Reaction on the Si (100) Surface. *Japanese Journal of Applied Physics*, 40(Part 1, No. 6B):4384–4387, June 2001.

[87] J. S. Montgomery, T. P. Schneider, R. J. Carter, J. P. Barnak, Y. L. Chen, J. R. Hauser, and R. J. Nemanich. Morphology of Si (100) surfaces exposed to a remote H plasma. *Applied Physics Letters*, 67(15):2194, 1995.

[88] A. Reina, X. Jia, J. Ho, D. Nezich, H. Son, V. Bulovic, M. S Dresselhaus, and J. Kong. Large Area, Few-Layer Graphene Films on Arbitrary Substrates by Chemical Vapor Deposition. *Nano Letters*, 9(1):30–35, January 2009.

[89] K. T. Chan, J. B. Neaton, and M. L. Cohen. First-principles study of metal adatom adsorption on graphene. *Physical Review B*, 77(23):235430, June 2008.

[90] P. Giannozzi, et al. QUANTUM ESPRESSO: a modular and open-source software project for quantum simulations of materials. *Journal of Physics: Condensed Matter*, 21(39):395502, September 2009.

[91] J. P. Perdew, K. Burke, and M. Ernzerhof. Generalized Gradient Approximation Made Simple. *Physical Review Letters*, 77(18):3865–3868, October 1996.

[92] Private communication with Liang Yang.